

THE DYNAMICS OF BLACK HOLES IN THE FIRST GALAXIES

A Dissertation
Presented to
The Academic Faculty

By

Chao Shi

In Partial Fulfillment
of the Requirements for the Degree
Doctor of Philosophy in the
School of Physics

Georgia Institute of Technology

August 2017

Copyright © Chao Shi 2017

THE DYNAMICS OF BLACK HOLES IN THE FIRST GALAXIES

Approved by:

Dr. John H. Wise, Advisor
School of Physics
Georgia Institute of Technology

Dr. Tamara Bogdanović
School of Physics
Georgia Institute of Technology

Dr. Laura Cadonati
School of Physics
Georgia Institute of Technology

Dr. Deirdre Shoemaker
School of Physics
Georgia Institute of Technology

Dr. Richard Vuduc
School of Computational Science
and Engineering
Georgia Institute of Technology

Date Approved: May 04, 2017

ACKNOWLEDGEMENTS

First and foremost, I would like to thank my adviser, John Wise, for his guidance throughout my graduate career. He provided me with ideas, and support, consideration, and always helped keep me on track. The research that composes this thesis would not have been possible without him. I thank my thesis committee, Tamara Bogdanović, Deirdre Shoemaker, Laura Cadonati, and Richard Vuduc, for their comments and involvement in this thesis.

I'd also like to thank my group members, Daegene Koh, Qi Ge, Kirk Barrow, Gabriel Altay, and Aycin Aykotalp that have spent joyful time with me. I thank all the professors here in School of Physics and College of Computing who have imparted knowledge and experience to me. I thank all the supporting staff here in Tech who made the transition of my life from China to U.S. as easy as possible.

I could not have made it through the seven years without some entertainment outside the office. I thank all the friends in the our badminton gang, Hongyu Guo, Yitao Liu, Baoyu Liu, Zunlong Ke, Ting Fang, Shilu Fu, Daquan Feng, Chunlong He, Zhenkun Wu, Xunzhe Xie and many more, with whom I play hours of badminton every week and gather together every now and then.

I would like to thank my parents for supporting me in whatever I love to do, and encourage me to fight for it without worrying about failure. Without their support, both financially and spiritually, I could not have made this far.

TABLE OF CONTENTS

Acknowledgments	v
List of Tables	ix
List of Figures	x
Chapter 1: Introduction	1
1.1 History of Black Holes	1
1.1.1 Theory	1
1.1.2 Observations	3
1.2 The physics of black hole formation	6
1.2.1 Structure formation	6
1.2.2 Pathways of black hole formation	13
1.3 Modeling Black Hole Growth in the Early Universe	20
1.3.1 Semi-analytical modeling	20
1.3.2 Cosmological numerical simulations	22
1.3.3 Current understanding of high-redshift black hole formation and growth	24
1.4 Overview of thesis	25
Chapter 2: Computational and Numerical Methods	26

2.1	Cosmological simulation code: Enzo	26
2.1.1	Physical equations	26
2.1.2	Numerical methods	28
2.2	Halo Finding	31
2.2.1	Friends-of-friends Method	32
2.2.2	HOP Method	33
2.2.3	Rockstar Method	34
Chapter 3: Simulation Setup		36
3.1	Cosmology parameters	36
3.2	Radiative cooling	36
3.3	Molecular hydrogen dissociating background	37
3.4	Star formation	39
3.4.1	Pop III Stars	39
3.4.2	Pop II stars	41
3.5	Stellar feedback	41
3.5.1	Pop III stellar feedback	43
3.5.2	Pop II stellar feedback	44
Chapter 4: Orbital Mechanics		45
4.1	Orbital analysis	45
4.1.1	Point mass approximation	45
4.1.2	Using the simulated gravitational potential	46
4.2	Dynamical Friction	50

Chapter 5: Results	53
5.1 Formation of stellar-mass black holes	53
5.2 Distribution of black holes within the first galaxies	56
5.3 Black hole orbital properties	60
5.3.1 Halo point mass approximation	60
5.3.2 Using the simulated gravitational potential	63
5.3.3 Angular momentum	69
Chapter 6: Conclusions and Future Work	73
6.1 Conclusions	73
6.2 Future work	74
References	83
Vita	84

LIST OF TABLES

3.1	Fractional metal-free stellar endpoints	40
-----	---	----

LIST OF FIGURES

1.1	Possible routes for massive black hole formation	15
1.2	A schematic diagram of a halo merger tree	20
2.1	Adaptive timestepping in a W-cycle	29
3.1	Lyman-Werner background evolution	38
4.1	Slices of gas density and gravitational potential	47
4.2	A comparison of the gravitational potentials	48
5.1	The total number of black hole remnants	54
5.2	Halo masses vs halo with BHs masses	56
5.3	Number of BHS vs halo masses	57
5.4	Evolution of radial distribution of black holes	58
5.5	The radial distribution at four different redshifts	59
5.6	Evolution of semi-major axis	61
5.7	Distribution of orbital semi-major axes in point source approximation	62
5.8	Distribution of orbital eccentricities in point source approximation	63
5.9	Evolution of semi-major axis in simulated potential	64
5.10	Distribution of orbital semi-major axes	65

5.11	Distribution of orbital eccentricities	66
5.12	Semi-major axes vs eccentricity	67
5.13	Distribution of kinetic to potential energies	68
5.14	Example of evolution of angular momentum	72

SUMMARY

Black holes (BHs) as massive as $10^9 M_\odot$ has been discovered at redshift $z > 6$, that is within one billion years after the big bang. It is believed that some seed black holes with large initial masses formed at very early times, which then grow to the supermassive black holes we observe at $z \sim 6$. First stars (Pop III) remnants are considered to be one of the promising pathways to form such seed BHs. We study the dynamics of seed BHs formed out of Pop III star remnants through cosmological simulation. We evolve a representative volume across 1Mpc in comoving coordinates, and write 1000 outputs every ~ 0.5 Myr. We then extract all seed BHs in each output and investigate the distribution and evolution of their orbital properties from redshift $z \sim 17$ to $z \sim 9$, which are crucial to their growth and merger rate. We show that most of seed BHs in halos are gravitationally bounded, and a significant fraction of them have orbits with short semi-major axes and high eccentricity. They are prime candidates for black hole mergers as they are the ones that will venture closest to the halo center and any massive black hole that might exist in the (proto-)galaxy center. We attempt to estimate the merger rate of BHs by calculating the loss rate of angular momentum, but find that this approach is not suitable for our simulation data. We propose a possible remedy for angular momentum calculation in the end. This work is the first so far to study BH evolution in full cosmological simulation on a sample large enough to draw statistical conclusions.

CHAPTER 1

INTRODUCTION

1.1 History of Black Holes

1.1.1 Theory

Pursuing the idea that gravity acts on light, British natural philosopher John Mitchell envisioned the existence of “dark stars” in a paper published in 1783. Starting with escape velocity, $v_e = \sqrt{2GM/r} = r\sqrt{8\pi G\rho/3}$, where r and ρ are the radius and density of the star, and he realized that increasing a star’s radius with constant density would increase the escape velocity. When the escape velocity exceeds the speed of light, all the light emitted by the star would be pulled back, thus no distant observer could see it. Such a star would become essentially invisible at a distance. However, probably due to the increasing popularity of theory of light as a wave, the development of this idea was paused. It was unclear how waves could interact with gravity.

The breakthrough came shortly after Albert Einstein formulated his theory of general relativity in 1915 (one of the many reasons why this is a scientific milestone in history), when Karl Schwarzschild obtained the first analytical solution of Einstein’s field equations for a non-rotating spherical star, now known as the Schwarzschild metric:

$$ds^2 = -c^2 d\tau^2 = -\left(1 - \frac{r_s}{r}\right) c^2 dt^2 + \frac{dr^2}{1 - r_s/r} + r^2(d\theta^2 + \sin^2 \theta d\phi^2) \quad (1.1)$$

where $r_s = 2GM/c^2$ is the Schwarzschild radius of the star with mass M . Here τ and t are the proper time and the time coordinate; r , θ , and ϕ are the radial and angle coordinates, and c is the speed of light. At the Schwarzschild radius from the center of the star, light emitted from the surface would have an infinite gravitational redshift, and therefore infinite time

dilation. Schwarzschild concluded that such star would be undetectable by an observer at any distance from the star since any signal within the Schwarzschild radius could not come out of the Schwarzschild sphere due to the infinite gravitational redshift. However, without the knowledge of how a real star could reach this critical radius at the time, most theorists were skeptical with this proposition, including Einstein himself.

This problem was solved quite serendipitously in the 1930s through a series of seminal work. It was started by Subrahmanyan Chandrasekhar when he set himself to derive the structure of white dwarfs. Combining the theory of stellar polytropes [1] and Fowler's equation of state for a non-relativistic degenerate electron gas, Chandrasekhar found that the radius (thus density) of a white dwarf star is proportional to the inverse cubic root of its mass: $r \sim M^{-1/3}$. Applying this relation on Sirius B, however, he discovered that a white dwarf star of $1M_{\odot}$ would have high enough density in its core to push the electron gas into fully relativistic regime, which invalidates Fowler's equation of state. He then relaxed the non-relativistic constraint to include relativistic momentum of the electrons, and deduced that the pressure's dependence on electron density softens from Fowler's $N_e^{5/3}$ to $N_e^{4/3}$. This seemingly little change, however, resulted in a bizarre conclusion that a fully relativistic polytropic gas can only be in equilibrium for a mass of precisely $0.91M_{\odot}$ (later corrected to be $1.4M_{\odot}$ by improved calculations, e.g. Harwit 1998), independent of its radius and density. This work was published in 1931, in which Chandrasekhar interpreted this value as the maximum mass attainable by a white dwarf star as it approaches fully relativistic degenerate conditions. One year later, the Russian physicist Lev Davidovic Landau obtained a similar result in the context of degenerate neutron stars, and went on to claim that stars beyond this limit would shrink in free fall, collapse to a point in the end — a singularity arises. The physical picture are simple: electrons and neutrons are both fermions. According to Pauli's exclusion principle and Fowler's equation, quantum degeneracy pressure would balance the gravitational pressure for stars within Chandrasekhar's limit. When the stars get more massive beyond the Chandrasekhar limit, additional gravitational pres-

sure lead to further contraction and therefore high enough core densities to push the kinetic energy at the top of the Fermi sea to levels comparable to the rest energy of the particles — the gas becomes relativistic. As mentioned above, the equation of state would soften from $N_e^{5/3}$ to $N_e^{4/3}$, where N_e is the number density of electrons, so the increase in quantum pressure slows down and always less than the increase of gravitational pressure, thus the contraction can not be stopped until shrink into a singularity.

After more detailed study of equilibrium configuration of white dwarfs [2] and neutron stars [3], in 1939, Oppenheimer and Snyder laid the foundation for the brand new field of physics about gravitational singularities in “On Continued Gravitational Contraction”. They obtained an analytical solution for the collapse of a cloud of gas by applying the general relativistic field equations to a sphere of cold neutrons, and demonstrated how collapsed objects are ideal test ground for a fully relativistic theory of gravity. The concept of black hole as we have today, were born, although the term “black hole” had not appeared until John Wheeler coined it two decades later in 1960.

1.1.2 Observations

In his paper “Nuclear Emission in Spiral Nebulae” published in 1943 [4], Carl Seyfert identified 12 galaxies with abnormal nuclei which have “high excitation nuclear emission lines superposed on a normal G-type spectrum”. For two of the galaxies identified, NGC 3516 and NGC7469, the broadened profiles of hydrogen emission lines indicated that the proper motion of gas inside their nuclei had velocities up to 8500 km s^{-1} . A supernova explosion was the only known source that can generate a flow of this magnitude in our own galaxy. Another anomaly of these galactic nuclei observed by Seyfert was their high luminosity, comparable to a whole galaxy. For example, the nucleus of NGC 4151 has about 70% of the luminosity of M 31 in the near ultraviolet. Not only bright, observations of variability timescales later also showed that these nuclei were compact, many of them were smaller than a few light minutes.

However, at the time, it was not realized that these super bright and compact active galactic nuclei (AGNs) were powered by central black holes. Seyfert's work also had not drew much attention until 1950s, when several newly discovered radio sources provided strong evidence that there was some new and extraordinary processes in the nuclei of these galaxies. The most unambiguous example was M87 from Virgo cluster. In 1954, Baade and Minkowski first suggested that the nucleus of M87 was the source of radio emitting plasma based on a bright narrow optical jet and unusual spectra of the ionized gas from the nucleus. 40 years later, M87 was the first galaxy confirmed to host a supermassive black hole in the center by the Hubble Space Telescope [5, 6].

M87 was not an isolated case. In the same year, Baade and Minkowski identified Cygnus A as one of the strongest radio sources in the sky, and its nucleus also showed strong extended emission like M87. Applying the newly developed theory of synchrotron radiation from a relativistic plasma (Shklovski, 1954) to the observed power law spectrum, luminosity and volume of Cyg A, the minimum energy in the relativistic electron and magnetic field was estimated to be 4×10^{58} erg, equivalent to the rest mass energy of $11000 M_{\odot}$. It can be about 100 times greater if we include the contribution of the relativistic protons too. At the time, it was hard to imagine any classical power source could meet this requirement while residing in the relatively small nuclei.

This energy deficit became too big to ignore when quasi stellar objects (QSOs) were discovered in the 1960s. Almost a third of the high latitude radio sources were QSOs. The brightest one has about 1000 times of the luminosity of the Andromeda galaxy. Moreover, some of the QSOs were proved to have size less than 1 pc by showing a variability on timescales of order of 1 year [7, 8, 9]. In 1970s, the newly launched X-ray telescope orbiting in space discovered that AGNs are luminous source of X-rays. More importantly, it observed that the luminosity some AGNs can change by factors of 2 within days, hours and even minutes, and thus put a even tighter constraint on the sizes of the central engine.

Since the discovery of QSOs, speculation about how the luminosity of these brightest

objects in the sky could be generated within such a small region initially concentrated on runaway explosions triggered by supernovae explosion in a tightly packed star cluster [10], the collapse and disintegration of a massive star with $10^5 - 10^8 M_\odot$ [11], rapid star formation in an infant galaxy [12], and galaxy collisions [13]. But none of these models seemed natural and simple enough. On the other hand, the idea that the energy source was gravitational became more and more popular after a series of pioneering work. John Wheeler, who popularized the term of “black hole”, first envisioned a gravitational singularity at the center of a galaxy, converting the matter that falls onto it to energy. A more detailed description of this process was given by Zel’dovich and Novikov [14] and Salpeter [15]. Lynden-Bell [16] attempted to explain the exotic properties of QSOs and Seyfert galaxies directly in terms of a black hole formalism.

Despite the promising theory developed so far, the single most important event that lead to the acceptance black holes as the power source was probably the discovery of pulsars by Jocelyn Bell in 1967 [17], when she was still a graduate student in University of Cambridge. Her work cleared the prevailing skepticism about the existence of neutron stars. With the presence of a critical mass above which neutron star could not stay in equilibrium, a stellar-mass black hole is the inevitable fate of such stars. Such stellar mass black hole was first detected when the mass of the rapidly varying X-ray source Cygnus X-1 was proven to be greater than the critical mass of a neutron star [18, 19, 20, 21].

In 1974, using then-new 35km baseline radio interferometer, Balick and Brown [22] discovered the point-like radio source at the center of our Milky Way Galaxy in the direction of constellation of Sagittarius, named Sagittarius A* (Sgr A*) 8 years later by Brown. Since then, numerous observations of the orbits and proper motions of stars in the vicinity of Sgr A* strongly suggest the radio source is a supermassive black (SMBH) hole weighing $2 - 4 \times 10^6 M_\odot$ [23, 24] looked further away into other nearby galaxies, we found similar evidence indicating that SMBHs with masses ranging from 10^6 to $10^9 M_\odot$ ordinarily dwell in their centers. Moreover, the masses of the central black holes are observed to have strong

correlations with their host galaxy spheroids properties, such as velocity dispersion (a.k.a. $M - \sigma$ relation [25, 26, 27, 28], mass [29, 30], luminosity [31], or other host properties. This is a rather surprising relation since the gravitational reach of the central black holes is rather small with respect to the sizes of their host galaxies. Since the launch of Sloan Digital Sky Survey (SDSS) in 2000, the number of detected quasars has been increasing rapidly. On the other hand some very bright quasars estimated to be powered by central black holes weighing $10^9 M_\odot$ are observed at high redshift ($z > 6$). Up to now the furthest quasar was observed at $z \approx 7.085$, which is just about 1 billion years after the big bang, less than 10% of current cosmic age, discovered in the United Kingdom Infrared Deep Sky Survey (UKIDSS) Large Area Survey (LAS) [32] by Mortlock et al. [33]. Further observation on this quasar showed that the central black hole has a mass of $(2 - 3) \times 10^9 M_\odot$. Adding to the surprise of tight correlation between central black holes and host galaxies, how SMBHs as massive as $10^9 M_\odot$ formed in less than a billion years is an open question.

1.2 The physics of black hole formation

The observed tight correlation between central black holes and host galaxies indicates there might be common root between galaxies and MBHs formation. To determine how these relationships have arisen and especially how SMBHs formed so fast, we must look into the early universe, and study black hole formation under cosmological context. In this section, I will briefly review the current theory about black hole formation and related cosmological background.

1.2.1 Structure formation

In current Cold Dark Matter (CDM) cosmology, matter in the universe right after the big bang is a smooth hot soup with very small density fluctuations arising from quantum effects. While the universe has been cooling down due to expansion, the small perturbations in density started to grow due to gravitational instability. The early universe can be con-

sidered as ideal fluid, which is described by continuity equation (mass conservation), Euler equation (fluid dynamics), Poisson equation (gravity), and equation of state (relates pressure and density). Combining the four equations mentioned above, the linearized equation describe the perturbation growth reads:

$$\frac{d^2\delta_k}{dt^2} + 2\frac{\dot{a}}{a}\frac{d\delta_k}{dt} = \left(4\pi G\bar{\rho} - \frac{k^2 c_s^2}{a^2}\right)\delta_k - \frac{2\bar{T}}{3a^2}k^2 S_k \quad (1.2)$$

Quantities with subscript k denotes the k th mode of the Fourier transformation of this quantity. $\bar{\rho}$ is the average density of the universe, and $\delta(x) = (\rho(x) - \bar{\rho})/\bar{\rho}$ is the density contrast against the average density of the whole universe. S is the entropy. The second term on the left expresses how the expansion suppresses the growth of perturbation. $4\pi G\bar{\rho}$ on the right hand side is the source of growth, while $k^2 c_s^2/a^2$ and the last term expresses how pressure due to spatial gradients and entropy influence the growth of perturbation.

To illustrate how gravitational instability operates, let's consider a simple case where the expansion of the universe and the entropy are dropped. The equation (1.2 is reduced to a wave equation:

$$\frac{d^2\delta_k}{dt^2} = -\omega^2\delta_k, \text{ where } \omega^2 = \frac{k^2 c_s^2}{a^2} - 4\pi G\bar{\rho} \quad (1.3)$$

$\omega^2 = 0$ defines a characteristic scale mode k_J , which further defines a characteristic scale,

Jeans length:

$$\lambda_J = a(t)\frac{2\pi}{k_J} = c_s\sqrt{\frac{\pi}{G\bar{\rho}}} \quad (1.4)$$

Then we have the **Jeans criterion:**

$$\lambda < \lambda_J \Rightarrow \omega^2 > 0 \Rightarrow \delta_k(t) \propto e^{\pm i\omega t} \text{ wave, propagate w. sound speed} \quad (1.5)$$

$$\lambda > \lambda_J \Rightarrow \omega^2 < 0 \Rightarrow \delta_k(t) \propto e^{\pm\omega t} \text{ static, decaying or growing exponentially} \quad (1.6)$$

This solution shows that on scales greater than Jeans length, the pressure can not balance the self-gravity, which means for over(under)-dense region the density perturbation will

grow (decay) exponentially with time. Considering the universe is expanding sub-horizon perturbation above Jeans length will grow slower in power law due to Hubble drag, while super-horizon perturbation froze after inflation because, in reality, it has no causal knowledge of the metric on scales larger than itself.

Given Jeans length, we can also define **Jeans mass**:

$$M_J = \frac{4\pi}{3} \bar{\rho} \left(\frac{\lambda_J}{2} \right)^3 = \frac{\pi}{6} \bar{\rho} \lambda_J^3 \quad (1.7)$$

At matter-radiation equality (t_{eq}), $M_J = 1.5 \times 10^{16} (\Omega_{\text{b},0} h^2)^{-2} M_{\odot}$. After recombination (t_{rec}), $M_J = 1.5 \times 10^5 (\Omega_{\text{b},0} h^2)^{-2} M_{\odot}$. The huge drop is because at recombination, photons decouple from baryons, which dramatically reduces the pressure.

Combining how average density scales with scale factor given by Friedmann equation, we have the following qualitative description of evolution of Jeans length:

$$t < t_{\text{eq}} \Rightarrow \bar{\rho} \propto a^{-4}, c_s \propto a^0 \Rightarrow \lambda_J \propto a \quad (1.8)$$

$$t_{\text{eq}} < t < t_{\text{rec}} \Rightarrow \bar{\rho} \propto a^{-3}, c_s \propto a^{-1/2} \Rightarrow \lambda_J \propto a^0 \quad (1.9)$$

$$t > t_{\text{rec}} \Rightarrow \bar{\rho} \propto a^{-3}, c_s \propto a^{-1} \Rightarrow \lambda_J \propto a^{-1/2} \quad (1.10)$$

We see that before matter-radiation equality time, the baryons are coupled with the photon fluid, thus the Jeans length grows with scale factor, and stays roughly constant between matter-radiation equality to recombination. Thus for baryons alone, there is perturbation growth in scales smaller than Jeans length. Moreover, since the coupling is imperfect before decoupling, there is damping of perturbations in the photon distribution, causing further damping through acoustic oscillations in baryons. This mechanism is known as Silk damping, with a characteristic scale defined as a typical distance photon can diffuse in Hubble time:

$$\lambda_d = \left(\frac{ct}{3\sigma_{\text{T}} n_e} \right)^{1/2} \quad (1.11)$$

If matter is purely baryonic, and perturbations are isentropic (no entropy as source, just density fluctuation) structure formation will only proceed through the fragmentation of perturbation larger than the Silk damping scale at recombination, with a typical mass $M_d \sim 10^{13} M_\odot$. Then the structure formation would continue in a “top-down” fashion, inconsistent with current observations. Also to allow sufficient time for fragmentation at this magnitude, the large-scale perturbations need large amplitudes in order to collapse early enough, which requires $|\delta_m| > 10^{-3}$ at recombination. Since the perturbations are isentropic, $\rho_r \propto T^4 \Rightarrow \delta_T = 1/4\delta_r = 1/3\delta_m \Rightarrow \Delta T/T > 10^{-3}$. This contradicts the CMB observation that $\Delta T/T \sim 10^{-5}$. Isothermal perturbation can eliminate the problem of Silk damping, thus allowing structure formation to proceed hierarchically (bottom up). However it would also result in large temperature fluctuations in CMB.

Now we see the necessity of dark matter. Since dark matter is collisionless, it does not obey the Euler equation. The Collisionless Boltzmann Equation (CBE)

$$\frac{\partial f}{\partial t} + \frac{\mathbf{p}}{m} \cdot \nabla f + \mathbf{F} \cdot \frac{\partial f}{\partial \mathbf{p}} = 0 \quad (1.12)$$

which is also known as the Vlasov equation, is required to describe its evolution in phase space f , where \mathbf{p} is the particle momentum and \mathbf{F} is some external force. However, a collisionless fluid with isotropic and homogeneous velocity dispersion can be described by the same continuity and momentum equations as a real fluid, but with sound speed c_s replaced by velocity dispersion $\sigma = \langle v_i^2 \rangle^{1/2}$. Thus we can also define Jeans length for dark matter:

$$\lambda_J = \sigma \sqrt{\frac{\pi}{G\bar{\rho}}} \quad (1.13)$$

Instead of Silk damping, dark matter perturbations below Jeans length will undergo free streaming damping, caused by velocity dispersion. According to its definition, we can estimate the Jeans length of dark matter from the typical velocity of a dark matter particle. As of today, the physical nature of dark matter is still unclear. There is still some current debate

over whether dark matter particle is relativistic (hot dark matter, HDM), non-relativistic (cold dark matter, CDM), or somewhere in between (warm dark matter, WDM). We define the free-streaming length as comoving distance traveled by a dark matter particle up to the time of matter-radiation equality.

$$\lambda_{\text{fs}} = \int_0^{t_{\text{eq}}} \frac{v(t')}{a(t')} dt' \quad (1.14)$$

For HDM, $v \sim c$, we get $\lambda_{\text{fs}} \sim 30$ Mpc, the corresponding free-streaming mass is $M_{\text{fs}} \sim 1.3 \times 10^{15} M_{\odot}$. So structure formation in HDM cosmology proceeds top-down. This is why current cosmology theory prefers CDM, which has a negligible free-streaming mass around the mass of Earth. With CDM at play, baryons can fall into the potential well formed by dark matter halo formed in bottom-up fashion, thus comprise the small scale fluctuation before recombination. This is now the widely accepted starting point of how galaxies are formed.

As discussed above, the baryonic Jeans mass right after recombination is $\sim 10^6 M_{\odot}$, so the baryons are expected to cluster in the same way as collisionless dark matter particles when the perturbations on galaxy scales are still in linear regime. When perturbations evolve into nonlinear stage and overdense regions start to collapse, unlike collisionless dark matter, baryons will be shock-heated when flow lines of the infalling gas converges, i.e., when gas is shocked. We can assume that the shock thermalizes all the kinetic energy of the gas cloud, and the internal energy of infalling gas can be ignored. Then the internal energy of the shocked gas is equal to the kinetic energy of the gas at infall. Assume the gas is mono-atomic, for which the adiabatic index $\gamma = 5/3$:

$$E_{\text{int,sh}} = \frac{3}{2} N k_{\text{B}} T_{\text{sh}} = \frac{1}{2} M_{\text{gas}} v_{\text{in}}^2 \quad (1.15)$$

$$\Rightarrow T_{\text{sh}} = \frac{\mu m_{\text{p}}}{3 k_{\text{B}}} v_{\text{in}}^2 \quad (1.16)$$

where, $N = M_{\text{gas}}/(\mu m_{\text{p}}$ is the number of gas particles. If the gas falls in from large

distance and has negligible initial velocity, then

$$v_{\text{in}} \approx v_{\text{esc}}(r_{\text{sh}} = \sqrt{2|\Phi(r_{\text{sh}})|}) \quad (1.17)$$

It is customary to equate the shock radius to what is known as the virial radius, giving

$$v_{\text{in}}^2 \approx \frac{GM_{\text{vir}}}{r_{\text{vir}}} = V_{\text{vir}}^2 \quad (1.18)$$

Then the temperature of the shocked gas in a halo with virial velocity is

$$T_{\text{sh}} \approx \frac{\mu m_{\text{p}}}{3k_{\text{B}}} V_{\text{vir}}^2 \quad (1.19)$$

If we further assume the halo has spherical symmetry and the gas is non-radiative, then when the shocked gas settle in hydrostatic equilibrium, $\Delta P(r) = -\rho_{\text{gas}}\Delta\Phi(r)$. Then combining the relation between potential Φ and temperature T_{sh} above, we obtain a relation between the total mass profile of the halo, temperature profile and gas density profile:

$$M(r) = M_{\text{gas}}(r) + M_{\text{DM}}(r) = -\frac{k_{\text{B}}T(r)r}{\mu m_{\text{p}}G} \left[\frac{d \ln \rho_{\text{gas}}}{d \ln r} + \frac{d \ln T}{d \ln r} \right] \quad (1.20)$$

For stars to form in the gaseous halo, cooling mechanism is necessary for the gas to radiate away heat so that gravitational contraction can overcome the thermal pressure and lead to further collapse on smaller scale. The primary cooling processes relevant for galaxy formation are two-body radiative processes. Gas loses energy by emitting photon after two-body interactions. There are mainly four types of two-body interactions:

Bremsstrahlung occurs when free electrons are accelerated by ions. According to Maxwell's equations, charge particles emit photons when accelerated.

Recombination occurs when free electrons recombine with ions. Binding energy and the kinetic energy of the free electron are both radiated away.

Collisional ionization occurs when free electrons collide with an atom, ionizing the atom.

The ionization takes away the kinetic energy of the free electron.

Collisional excitation occurs when a free electron knocks a bound electron to an excited

state. When the excited electron decays back to ground state later, it emits a photon.

We see that all 4 types of cooling process need free electrons, and all but bremsstrahlung also need neutral atoms or to form neutral atom. At high temperature, above a few times 10^7K , gas is fully ionized (for primordial gas this threshold is 10^6K). The only significant effect is bremsstrahlung. At $T < 10^{5.5}\text{K}$, a large fraction of the electrons are bound to their atoms, so the dominant cooling process is collisional excitation followed by radiative de-excitation. At temperatures below 10^4K , most of the electrons are bound to their atoms, and radiative cooling rates drop dramatically. The cooling is mainly accomplished through chemically enriched gas.

In addition to collisional ionization, an atom can also be ionized through photoionization, absorbing a photon. An external radiation field can thus change the population of ions, thereby changing the cooling rate of gas. Moreover, photoionization can directly heat the gas when the surplus energy of the photon is transformed to the kinetic energy of the electron. Depending on the density, temperature, and intensity of external radiation field, the gas may be in a state of net cooling, thermal equilibrium, or net heating, depending on the competition of heating and cooling process.

All stars form in Giant Molecular Clouds (GMCs). Observations have shown that the structure of GMCs is extremely clumpy. They consist of molecular clumps, which further consist of molecular cores (a.k.a. proto-stellar cores). The mass of a typical GMC is $M = 10^5 - 10^6 M_\odot$, with number density $n = 100 - 500 \text{ cm}^{-3}$. For clumps and cores, these two numbers are $M = 10^2 - 10^4 M_\odot$, $n = 10^2 - 10^4 \text{ cm}^{-3}$ and $M = 0.1 - 10 M_\odot$, $n > 10^5 \text{ cm}^{-3}$, respectively. The lifetime of GMCs is of the order of $t_{\text{GMC}} \simeq 10^7 \text{ yrs}$, while the free-fall time of GMCs is about $t_{\text{ff}} = \sqrt{3\pi/32G\rho} \simeq 3.6 \times 10^6 \text{ yr}$. We see that free-fall time is significantly smaller than the lifetime for GMCs. This poses the question of how

does GMCs support itself against gravitational collapse. Current observations and theory suggest that GMCs are supported by supersonic turbulence. In the presence of turbulence, the Jeans mass of GMCs scales as

$$M_J \propto \frac{(c_s^2 + \sigma_v^2)^{3/2}}{\widehat{M}\rho^{1/2}} \quad (1.21)$$

where \widehat{M} is the Mach number, c_s is the sound speed, and σ_v is the velocity dispersion. Since $\sigma_v \propto R^{1/2}$, on large scales, $\sigma_v \gg c_s$, turbulent motions increase the effective pressure, suppressing gravitational collapse, thus preventing the whole GMC from forming stars. On the other hand, the Jeans mass is dominated on small scales ($\sigma_v < c_s$) by the sound speed c_s , thus local turbulent motions may cause local overdensities that surpass the Jeans mass, thus promoting collapse and star formation.

There still exist open questions on the formation of GMCs, though. Molecular gas can form wherever external pressure is sufficiently high and radiation intensity is sufficiently low. But this is not enough to explain the clumpiness of GMCs. It is believed that GMCs are formed through three types of instabilities, thermal, gravitational and Parker (magnetic buoyancy). These instabilities can be triggered by a wide range of processes such as accretion of matter, large scale turbulence, spiral arms of disk galaxies, star formation itself, and galaxy mergers and interactions.

1.2.2 Pathways of black hole formation

As mentioned in the first section, black holes as massive as $10^9 M_\odot$ have been discovered at redshift $z > 6$, that is within one billion years after the big bang. It is easy to understand why this is remarkable by estimating the growth time of a MBH. It is believed that usually, MBHs cannot accrete at rates significantly higher than allowed by the Eddington limit, which is the point when the luminosity of a source becomes large enough that radiation pressure balances gravitational force. The Eddington luminosity is written as

$L_{\text{Edd}} = M_{\text{BH}}c^2/t_{\text{Edd}}$, where $t_{\text{Edd}} = \sigma_{\text{T}}c/4\pi Gm_{\text{p}} = 0.45 \text{ Gyr}$, where σ_{T} is Thomson cross section and m_{p} is the proton mass. Assuming the efficiency of conversion of rest-mass into energy (radiation) is ϵ , inflow rate of mass toward the MBH is \dot{M}_{in} , we have

$$L = \epsilon\dot{M}_{\text{in}}c^2 = L_{\text{Edd}}c^2 \quad (1.22)$$

Then the growth time of an MBH with initial mass M_0 is

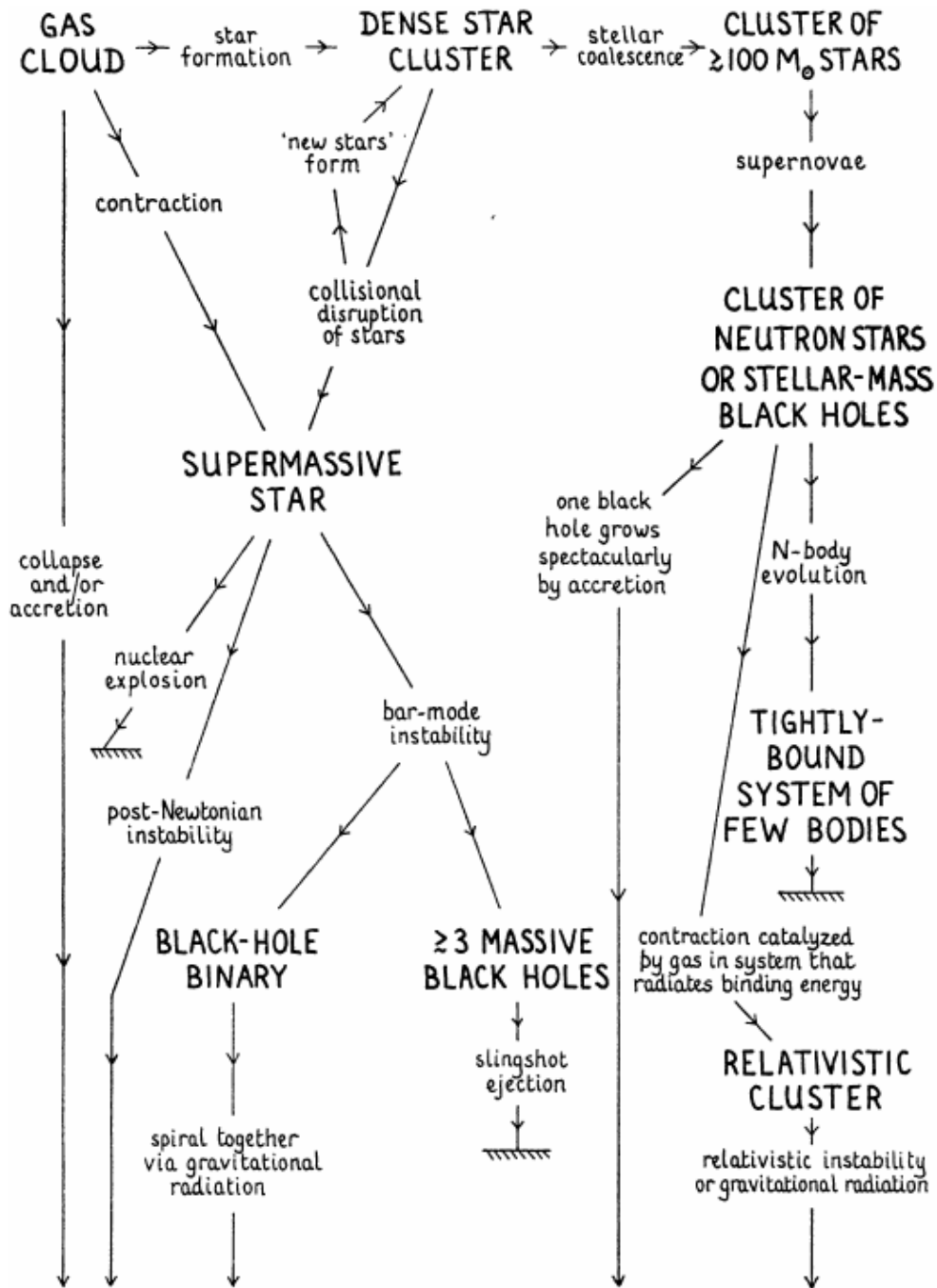
$$t_{\text{growth}} = t_{\text{Edd}} \frac{\epsilon}{1 - \epsilon} \ln \left(\frac{M_{\text{BH}}}{M_0} \right) \quad (1.23)$$

If the seed black hole is on the order of a solar mass, it needs to grow 9 orders of magnitude in about 1 Gyr. From the equation above we can see that it is possible only if the black hole accretes at the Eddington rate all the time, which means the feedback effects from stars and the MBH have to be negligible. But such a scenario is extremely rare with these SMBHs at $z \sim 6$ having a number density of $\sim 1 \text{ comoving Gpc}^{-3}$. It is then natural to assume that some seed black holes formed at the very early times and had large initial masses, which then grow to the supermassive black holes we observe at $z \sim 6$. There are several proposed scenarios for the formation of MBH seeds, reviewed in the following sections and illustrated in Figure 1.1.

Pop III star remnants

One of the popular proposed pathways for MBH formation is that MBH seeds form out of remnants of Pop III stars, i.e., the first generation of stars formed out of gas with zero metallicity. As discussed above, first stars are expected to form in minihalos, with $M_{\text{min}} \approx 10^6 M_{\odot}$. The virial temperature of these minihalos is $T_{\text{vir}} > 10^3 \text{ K}$, allowing cooling by molecular hydrogen.

Simulations of collapsing GMCs [35, 36, 37, 38] showed that the characteristic stellar masses are massive with $m_{\star} \simeq 30 - 300 M_{\odot}$ among the first generation of stars. The



massive black hole

Figure 1.1: Possible routes for massive black hole formation through remnants of massive metal-free stars, the collapse of dense stellar clusters, and the direct collapse of a gas cloud. Taken from Rees [34].

mass accreting rate in the hydrostatic protostellar core is $\sim 10^3$ times the observed local forming stars, indicating that first stars could indeed be very massive [39, 40, 41]. Massive stars usually have short lifetime, due to the enormous gravitational contraction and high luminosities. The final fate of first stars depends on their mass M_* .

($M_* = 25 - 140 M_\odot$) The remnants of first stars are predicted to collapse to black hole directly, with about half of the stellar mass going into the black hole [42]. If the formed black hole is not massive enough however, it might not stable enough to dwell at the center of the galaxy. Instead it might wander within its host and dynamically interact with the stars of similar mass.

($M_* = 140 - 260 M_\odot$) The Pop III stars explode in supernovae after death. In this mass range, when the helium burnt out, the temperature and density enter the regime in which electron/positron pairs are created, converting internal gas energy into rest mass and drastically reduce the pressure [43]. Without the support of pressure against gravity, the star will implode, leading to the burning of oxygen and silicon, which produces enough energy to reverse the collapse, triggering a supernova explosion and leaving nothing behind.

($M_* > 260 M_\odot$) The extreme temperature and density inside the star will trigger photodisintegration instability, where high-energy photons are absorbed by nuclei which then split into a lighter nuclei and subatomic particles, before the burning of oxygen and silicon core trigger explosion ([43]. When this instability occurs, it absorbs energy, reducing the temperature and pressure. The collapse of the core is thus catastrophic, leading to the formation of a seed black hole, with at least half of the initial stellar mass [44].

This path to MBH formation seems very natural. However, it is unclear if it really is a common process of forming a black hole seed because the initial mass function of Pop III stars is not constrained well enough. Furthermore, the binary fraction of this population

and how many stars form per minihalo are also unconstrained. The latter case will produce less massive first stars, given a constant star formation efficiency, as defined as the fraction of gas mass converted into stars. Even if single stars are formed in abundance, as mentioned before, simulations have shown that typically gas clumps with mass $\sim 10^3 M_\odot$ can collapse and form a very dense core of $\approx 0.01 M_\odot$ first. Afterward the gas around the core accretes rapidly onto the core, and eventually growing into the final main sequence Pop III star. Due to feedback during the protostellar phase, the final mass can be much less than the mass of the initial clump [45]. In short, currently it is uncertain whether or not there exists a non-negligible fraction that are very massive, and especially if they are above the threshold of $260 M_\odot$ to form MBH seeds.

Besides baryons, it has also been proposed that weakly interacting massive particles (WIMPs), one of the promising candidates for dark matter particles, may also form a type of “dark star”, which is supported by dark matter annihilation instead of nuclear fusion [46, 47]. The dark matter annihilation can be triggered if the dark matter halos have steep density profiles, so that baryonic infall during the star formation can compress the dark matter further adiabatically. It is estimated that dark stars have masses in the range $500 - 1000 M_\odot$, high luminosity ($10^6 - 10^7 L_\odot$), but low surface temperature ($< 10^4 K$). Such massive objects are also expected to collapse and form MBHs.

Direct collapse

Another way to form black holes is that a single clump of dense gas directly collapses into a massive black hole [48, 49, 50, 51, 52, 53, 54]. While it seems to be a natural way to form black holes, the physical conditions have to be in the regime where fragmentation and star formation is suppressed. The inner regions of gaseous proto-galaxies provides ideal locations for that due to the zero to very low metallicity of the primordial gas. Chemically enriched gas have more atomic transitions and are thus more efficient in cooling, facilitating fragmentation and star formation and reducing the amount of gas for black hole

formation. Besides metal cooling, H_2 cooling can also lead to fragmentation during the collapse. Suppressing H_2 formation in primordial galaxies requires a dissociating UV, so-called Lyman-Werner, background radiation.

In addition to suppressing fragmentation, the gas clumps need to have low intrinsic angular momentum and/or mechanisms to transport excessive angular momentum away. Global dynamical instabilities, such as the “bars-within-bars” mechanism which relies on global gravitational instability during a dynamical infall [55, 53] is a good candidate to shed angular momentum efficiently. Major galaxy mergers may also provide external torque on large scale to drive rapid gas inflow [56], in which case fragmentation may be inhibited by turbulence. Some idealized numerical simulations of gaseous disk in halos can lose up to 90% of its angular momentum due to supersonic turbulent motions, forming a compact but vertically thick disk supported by rotation that is marginally stable against gravitational instabilities.

The gas accumulates in the central few parsecs that can form a massive object of $10^4 - 10^6 M_\odot$. If the mass accretion proceeds slowly and less efficiently from this point, the condensed gas clump might form a supermassive star (SMS, $\gtrsim 5 \times 10^4 M_\odot$) first, and then collapse to black hole after its death. On the other hand, if the mass accumulation is fast, the condensed gas clump would form a more complex structure that consists a star (convective core) in the center and surrounded by a convectively stable envelope. An initial black hole of a few M_\odot would form as a result of core collapse after the star exhausts its fuel, and continued to grow through accretion from the bloated envelope. This stage is named “quasistar”, an initially low-mass black hole embedded in a massive envelope supported by radiation pressure [53, 57]. As mentioned in the beginning of this section, its growth is limited by the Eddington limit for the whole quasistar stage. The final massive seed would stop growing when the entire envelope is consumed. More detailed calculation of the mass accretion process show that the final seed MBHs would have masses in the range $10^4 - 10^5 M_\odot$ [58]

Collapse of dense stellar clusters

As mentioned in the direct collapse scenario, if H_2 forms in abundance, molecular cooling will facilitate the formation of Pop III stars in mini-halos ($T_{\text{vir}} < 10^4 K$, thus direct collapse is not possible since it is mutually exclusive with star formation). By the time more massive halos are built up through mergers, they will contain metal-enriched gas that is impacted by metal ejecta from Pop III supernovae. Enriched gas can fragment and cool more efficiently than primordial gas, and thus enable more efficient formation of “normal” stars. These stars can form very compact nuclear star clusters [59, 60] where star collisions can lead to the formation of a VMS, and thus may form a MBH remnant of $10^2 - 10^4 M_{\odot}$ [61]

The evolution of such collisional stellar systems is driven by dynamical interactions. As less bound stars running away from the center, the core radius will decrease due to energy conservation. Therefore the central density will increase and, as a result, the inner region relaxes faster than the outer region. Eventually the core will thermally decouple from outer region, where star-star collisions occur in the way of runaway collisions and leads to the formation of a VMS in a short timescale [62, 63].

Primordial black holes

The last but controversial candidate occurs very early in the cosmic timeline, before the epoch of galaxy formation. These are primordial black holes that also form out of high density fluctuations during the first minutes after the Big Bang. The masses of primordial black holes roughly equal the mass within the particle horizon at the redshift of their formation [64, 65], ranging from Planck Mass (formed at Planck epoch) to about $1 M_{\odot}$ (formed at the QCD phase transition) up to $10^5 M_{\odot}$ [66].

Some additional constraints can be applied to primordial black holes to narrow down their mass range. If the initial mass is less than 5×10^{14} g, the the primordial black holes are expected to evaporated due to Hawking radiation. For masses in the order of 10^{15} g, observed intensity of diffuse gamma ray background [67] suggests their contribution to

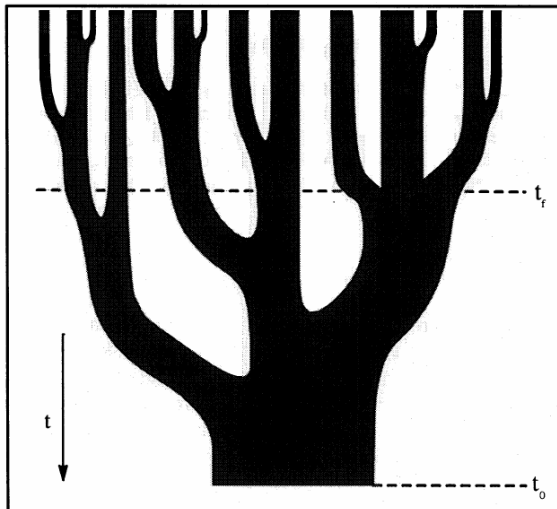


Figure 1.2: A schematic diagram of a halo merger tree with the width of the branches proportional to the halo mass. Galaxy and black hole semi-analytical models are build upon these types of merger trees. Taken from [71].

the matter density is less than 10^{-8} of the critical density. For larger masses, observation through micro-lensing techniques [68, 69] and spectral distortions of CMB [70] limit the mass to less than $\sim 10^3 M_\odot$

1.3 Modeling Black Hole Growth in the Early Universe

In order to study the evolution of black holes from their birth to present day, we must model black holes in cosmological background, and evolve them within their host galaxy and halo. In this section, I will review two popular modelling methods of galaxy and black hole formation and evolution – semi-analytical models and numerical simulations, along with an overview of the current state of the field concerning black holes at very high redshifts ($z \gtrsim 6$).

1.3.1 Semi-analytical modeling

Semi-analytical models of galaxy and black hole evolution describes the assembly history of a halo by its merger tree, which is typically built upon extended Press-Schechter formalism [72, 71] in a Monte Carlo manner. The random process is accomplished by calculating

the probabilities of the merger time and mass ratio of the last merger, creating two progenitor halos. Then the same calculation is performed recursively until some minimum halo mass is reached. A schematic of a merger tree is shown in Figure 1.2. Merger trees can also be extracted from cosmological dark matter simulations that serve as an alternative method, which contains the spatial and clustering information about the halos at an added computational cost [73]

Provided a merger tree, physically motivated recipes that describe physical processes, such as gas accretion, star formation and feedback, black hole growth and feedback, and stellar evolution, are used to evolve the galaxy and black hole within each halo in the merger tree [74]. These recipes start with the earliest and least massive progenitors of the target halo and evolve them forward in time, which is the reverse of the merger tree creation process. When generating production data, hundreds or thousands of merger tree realizations are generated in this Monte Carlo method to compile a multitude of statistics.

Furthermore, these recipes also consider specialized models for merging galaxies and the associated merger of the central massive black holes [75, 76]. They can also include any type of “kick” of the resulting black hole after a merger whose velocities average around a few hundred km s^{-1} [77, 78, 79]. The black hole growth and feedback model needs the user to specify a seeding mechanism (e.g. stellar-mass or direct collapse) the accretion rate (e.g. Eddington or Bondi), accretion disk properties (e.g. thin disk), and any physical trigger for accretion (e.g. galaxy mergers or various types of feedback).

After calculating the merger tree and applying a semi-analytical galaxy and black hole model, one obtains a history of the massive black holes that live within the progenitor halos, which can include formation rate, merger rate, ejection rate, growth rate, and the duty cycle [80].

1.3.2 Cosmological numerical simulations

Thanks to the exponential growth of computing power, modern cosmological simulations directly model the dark matter and gas dynamics of galaxy formation self-consistently in a large-scale environment with high dynamic scale. Sub-resolution models are then incorporated into the hydrodynamical framework to model the formation of stars and black holes and their subsequent feedback onto their environments through mechanical (supernovae for stars and jets for black holes) or radiative processes [81].

Simulations that focus on typical galaxies, such as the Milky Way, and more massive ones cannot resolve the halos that form the seed black holes. In this case, one assumes that halos with some pre-determined mass ($M_{\text{vir}} \sim 10^{10} M_{\odot}$) that are well-resolved by the simulation are seeded with a massive black hole with mass $\sim \text{few} \times 10^5 M_{\odot}$ that usually already follows the $M - \sigma$ relation [82, 83]. These simulations can reproduce the luminosity function of lower redshift quasars, which are generally not sensitive to the seeding mechanism [84] but cannot capture the physics of the seeding mechanism.

Simulations that can resolve the dark matter halos that possibly host black hole seeds formation can directly model black hole formation, through the three pathways discussed in Section 1.2.2. The maximal resolution of these simulations are hundreds of parsecs at best, which model the hydrodynamics on scales many orders of magnitudes greater than the Schwarzschild radius. Thus we can not simulate the feedback of black hole self-consistently (e.g., solving Einstein's field equations).

However in a uniform medium, the accretion onto the black hole can be described with Bondi-Hoyle accretion [85, 86] that assume spherical symmetry but provides the length scale in which gravity overcomes thermal pressure. This length scale is known as the Bondi radius,

$$r_b = \frac{GM_{\text{BH}}}{c_{s,\infty}} \simeq 0.1 \text{ pc} \left(\frac{M_{\text{BH}}}{100 M_{\odot}} \right) \left(\frac{T}{3000 \text{ K}} \right)^{-1} \quad (1.24)$$

where $c_{s,\infty} = \sqrt{\gamma k_B T / \mu m_p}$ is the sound speed at large distances (well outside r_b) and γ is the adiabatic index. The associated accretion rate is

$$\dot{M}_{\text{BH}} = 4\pi \lambda_B r_b^2 \rho_\infty c_{s,\infty} = 4\pi \lambda_B \rho_\infty \frac{G^2 M_{\text{BH}}^2}{c_{s,\infty}^3}, \quad (1.25)$$

where ρ_∞ is the gas density far outside r_b . Here λ_B is a dimensionless accretion rate that ranges from ~ 1.1 for an isothermal gas to $1/4$ for an adiabatic gas. The Bondi-Hoyle rate decreases if the ambient gas has a velocity v_{rel} relative to the black hole at a rate

$$\dot{M}_{\text{BH}} = 4\pi \lambda_B \rho_\infty \frac{G^2 M_{\text{BH}}^2}{(c_{s,\infty}^2 + v_{\text{rel}}^2)^{3/2}}, \quad (1.26)$$

Currently, only the small volume, high resolution cosmological simulations [87, 88] that focus on the seeding mechanisms can resolve the Bondi radius. Here the simulation takes the gas density and temperature of the gas element in which the black holes resides in Equation 1.26.

For larger simulations that cannot resolve this scale, the rate is multiplied by a “boost factor” $\alpha \sim 200$ that mimics a density gradient $\rho \propto r^{-\beta}$, where $\beta = 2$ for an isothermal sphere, below the resolution limit. The boost factor effectively connects the density in the coarse gas element to the unresolved Bondi radius [82, 89]. Bondi-Hoyle accretion rates are usually not allowed to exceed the Eddington rate. Other more simplified models use the Eddington rate with some radiative efficiency ϵ .

Once the accretion is known it is straightforward to convert it into a luminosity (Equation 1.22 that can be injected into the simulation medium through (i) thermal energy, (ii) radiation, or (iii) kinetic energy in a collimated jet. This energy will impact the surrounding regions as the (radiation) hydrodynamics solver incorporates this energy into the system [89].

1.3.3 Current understanding of high-redshift black hole formation and growth

Due to the lack of observations at very high redshifts, all seeding pathways have large uncertainties. However in Λ CDM cosmology, we can use these models to understand how the first stars, galaxies, and black holes form in the early universe given some reasonable guess of initial conditions.

The formation rate of stellar mass black hole seeds, which are the subject of this thesis, are directly tied to the Population III star formation rate [90]. Even more uncertain is the formation rate of direct collapse black holes, but the optimal physical conditions are being constrained to metal-free and highly-irradiated environments, such as an infalling, starless dark matter halo [91].

Concerning the stellar mass seeds, their stellar progenitors are massive stars, which heat and ionize the surrounding proper kpc through the absorption of far-ultraviolet radiation above the ionization potential $E = 13.6$ eV of hydrogen [92, 93, 94] After a few million years, typical gas densities and temperature are 1 cm^{-3} and 10^4 K, respectively.

Once the star dies, any possible black hole remnant will reside in a warm, diffuse and ionized region [87], which is hostile for accretion (see Equation 1.26. This suppression of prompt accretion lasts for tens of millions of years until “fresh” gas is supplied through cosmological smooth accretion or mergers [88]. Even if they exist in the center of their host halo, their growth is severely limited by radiative feedback. Alvarez [87] and Jeon [88] both found that a $100 M_{\odot}$ seed black hole grows less than one solar mass over ~ 100 Myr (as the halo grows by a factor of ~ 100) when radiative feedback is considered. Without its effects, the black hole can grow by a factor of 100.

To date, simulations only follow a handful of these stellar mass black holes and their feedback. They have always focused on the first star to form in the simulations, but very few have looked at the formation and evolution of the high-redshift population of these compact remnants.

1.4 Overview of thesis

The focus of this thesis is to characterize the formation and dynamics of the first black holes in the universe, stemming from metal-free Population III stars. We evolve a representative volume of the early universe including first black holes self-consistently by cosmological simulation, and investigate the distribution and time evolution of dynamical properties statistically from a sample of several hundred BHs.

We briefly review the numerical methods and software used to simulate black holes formation in a cosmological context and to analyze in post-processing these simulated data in Chapter 2. Then we describe the cosmological simulation setup and the physical recipes incorporated in the numerical framework in Chapter 3. In Chapter 4, we derive the analytical models used to extract orbital properties of black holes. Chapter 5 presents our results on various dynamical properties of black holes within the first galaxies. We conclude this thesis, along with discussing future work, in Chapter 6.

CHAPTER 2

COMPUTATIONAL AND NUMERICAL METHODS

2.1 Cosmological simulation code: Enzo

The simulation in this work is run in Enzo [95], a structured adaptive mesh refinement (SAMR) code originally developed for cosmological hydrodynamics. It has since been used on a wide variety of problems, and it has grown to become a general tool for astrophysical fluid dynamics. Here I summarize the key physical equations and sub-grid models relevant to this work. For a full description of Enzo, please refer to the methods paper [95].

2.1.1 Physical equations

The basic equations solved by Enzo are Eulerian equations of ideal magneto-hydrodynamics (MHD) including gravity, in a coordinate system comoving with the cosmological expansion.

$$\frac{\partial \rho}{\partial t} + \frac{1}{a} \nabla \cdot (\rho \mathbf{v}) = 0 \quad (2.1)$$

$$\frac{\partial \rho \mathbf{v}}{\partial t} + \frac{1}{a} \cdot \left(\rho \mathbf{v} \mathbf{v} + \mathbf{I} p^* - \frac{\mathbf{B} \mathbf{B}}{a} \right) = -\frac{\dot{a}}{a} \rho \mathbf{v} - \frac{1}{a} \rho \nabla \phi \quad (2.2)$$

$$\begin{aligned} \frac{\partial E}{\partial t} + \frac{1}{a} \nabla \cdot \left[(E + p^*) \mathbf{v} - \frac{1}{a} \mathbf{B} (\mathbf{B} \cdot \mathbf{v}) \right] = & -\frac{\dot{a}}{a} \left(2E - \frac{B^2}{2a} \right) \\ & - \frac{\rho}{a} \mathbf{v} \cdot \nabla \phi - \Lambda + \Gamma + \frac{1}{a^2} \nabla \cdot \mathbf{F}_{\text{cond}} \end{aligned} \quad (2.3)$$

$$\frac{\partial \mathbf{B}}{\partial t} - \frac{1}{a} \nabla \times (\mathbf{v} \times \mathbf{B}) = 0 \quad (2.4)$$

In above equations, E , ρ , v , and B are the comoving total fluid energy density, comoving gas density, peculiar velocity, and comoving magnetic field strength vector, respectively. The matrix I is the identity matrix, and a is the cosmological expansion parameter. The first three equations are conservation laws of mass, momentum, and total (kinetic, thermal, and magnetic) fluid energy. They are the first, second, and third moments of Boltzmann equation. Λ , Γ and F_{cond} in Equation 2.3 represent radiative cooling, radiative heating, and flux from thermal heat conduction, respectively. The fourth equation is the magnetic induction equation.

The comoving total energy density E is calculated as

$$E = e + \frac{\rho v^2}{2} + \frac{B^2}{2a} \quad (2.5)$$

where e is the comoving thermal energy density. The terms on the right hand side of the equation represent the thermal, kinetic, and magnetic energy density.

The total comoving isotropic pressure p^* is given by

$$p^* = p + \frac{B^2}{2a} \quad (2.6)$$

where p is thermal pressure. The terms on the right hand side represent the thermal and magnetic pressure components.

To complete the set of equations, we still need an equation of state and Poisson's equation for the gravitational potential ϕ :

$$e = \frac{p}{\gamma - 1} \quad (2.7)$$

$$\nabla^2 \phi = \frac{4\pi G}{a} (\rho_{\text{total}} - \rho_0). \quad (2.8)$$

We treat the gas as ideal gas with a ratio of specific heats γ . The source of gravitational

potential is total mass density contrast, where $\rho_{\text{total}} = \rho_{\text{gas}} + \rho_{\text{dm}} + \rho_{\text{stars}}$, and ρ_0 is the mean density.

2.1.2 Numerical methods

Structured Adaptive Mesh Refinement

Adaptive mesh refinement (AMR) is a technique to refine the mesh and timestep of the simulation where higher resolution is needed, which is highly suitable for cosmological simulation due to its extremely high dynamical range. Enzo employs Berger & Colella's structure AMR (SAMR) [96], which utilizes an adaptive hierarchy of grid patches at varying levels of resolution. Each grid covers some region of space requiring higher resolution than its parent grid, and can have one or more child grid of even higher resolution if necessary.

The grid hierarchy starts with a root grid, which is a coarse uniform Cartesian grid covering the whole volume of simulation. As the solution evolves, some regions of interest, e.g., regions with high density, start to form, which require higher resolution to accurately capture the physical detail. Then finer grids are placed within these coarse regions. Typically the ratio of cell sizes between parent and child grids are set to two or four, and all grids with the same cell size are defined as the same level.

The solution is advanced in a manner of a W-cycle (see Figure 2.1 in a multigrid solver. First, we determine the maximum timestep allowed for the coarsest grid given some accuracy and stability criteria and advance this grid by that time interval. We then move to the next level and advance all grids on this level for the same timestep. We repeat this procedure until we reach the bottom level of grid hierarchy and advance the finest grid patches until it is synchronized in time with the coarsest (root) grid.

Whenever a level has caught up to its parent level, all grids on this level and at finer resolutions will be rebuilt. The hierarchy rebuilding process is achieved by applying certain grid refinement criteria to grids on this level and flagging zones that require finer resolution.

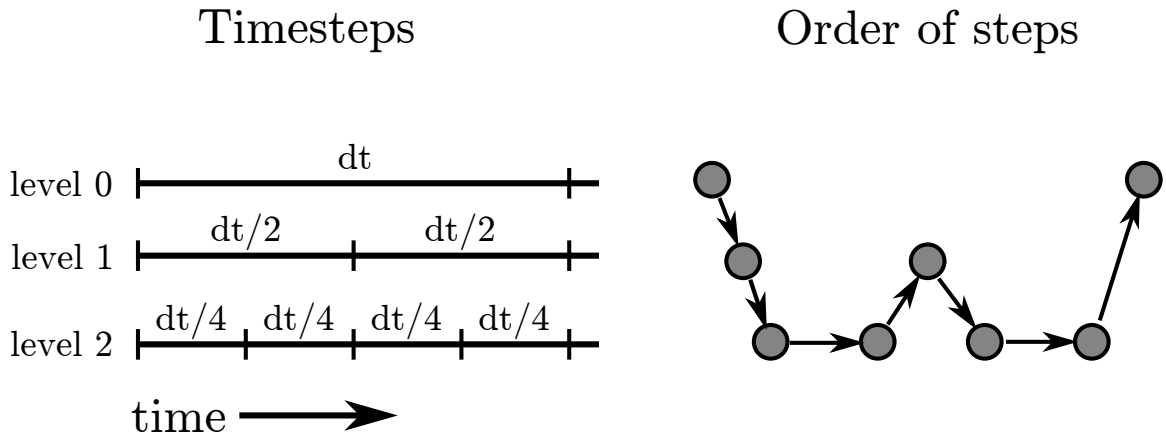


Figure 2.1: Left: An example where the timesteps on AMR levels are restricted by a factor of one-half, but Enzo does not necessarily place use this restriction, where the timesteps obey the CFL condition. Right: The “W-cycle” that depicted the order in which timesteps are taken in AMR grids on each level. Taken from [95].

The exact criteria applied depend on the physical problem being simulated, but usually the cells are flagged if the difference of some physical quantities of interest exceeds some threshold. Once a grid has a set of flagged cells, an algorithm based on computer vision [97] is applied to find edges and determine a good placement of subgrids. The initial value on these new subgrids will be interpolated from their parent grids. This whole procedure is then repeated recursively on the new grids until all levels of grids (old and new) are examined and no new level of grids needs to be built. In this way, the whole hierarchy is rebuilt.

(Magneto)-hydrodynamic Solver Methods

Four different (magneto)-hydrodynamic methods are implemented in Enzo: (1) the hydrodynamic only piecewise parabolic method (PPM) developed by Colella [98] and extended to cosmology by Bryan [99], (2) the MUSCL-like Godunov scheme [100] with or without magnetic fields and Dedner-based divergence cleaning [101, 102], (3) a constrained transport (CT) staggered MHD scheme [103], and (4) the second-order finite difference hydrodynamics method described in ZEUS [104, 105].

Gravity

Enzo employs the fast Fourier transformation (FFT) technique [106] to solve Poisson's equation on the root grid on each timestep. It is fast, accurate, and naturally allows both periodic and isolated boundary conditions for the gravity, which are commonly used in astrophysics and cosmology. On subgrids, we first interpolate the boundary conditions from the parent grid, then solve Poisson equation on one subgrid at a time with a multigrid technique.

N-body Dynamics

Dark matter and stars are modeled as collisionless matter, which is then modeled with particles that interact with the baryons only through gravity in the Enzo code. We utilize a drift-kick-drift algorithm [106] to advance these particles every timestep, which has second-order accuracy even in varying timesteps. Since the collisionless particles follow the collapse of structure, they are not adaptively refined, nor are there duplicate sets of particles for each level; instead, each particle is associated with the highest refined level available at its position, and particles are moved between grids as the hierarchy is rebuilt. Although the particles are fixed in mass once created (except for star particles, which can lose mass due to feedback), these particles can be created with any initial set of masses and positions.

Chemistry

Enzo uses a non-equilibrium chemical network, capable of tracking up to 12 particle species. The simplest model includes just atomic hydrogen and helium (H , H^+ , He , He^+ , He^{++} , e^-). More complicated models can include species related to gas-phase molecular hydrogen formation (H^- , H_2 , and H_2^+), and HD formation (HD , D , D^+). The cooling and heating due to these species are also modeled. The evolution of these species is described by rate equation, which is solved using one Jacobi iteration of an implicit Euler time discretiza-

tion to ensure stability. The rate equations are further sub-cycled within one hydrodynamic timestep to ensure accuracy.

Radiative Cooling and Heating

There are several modes of radiative cooling and heating built in Enzo. The simplest mode computes the cooling rate from a simple temperature-dependent cooling function [107] without considering any differences between cooling and heating effects between different chemical species. When the chemistry is turned on, the code can include cooling from all species of hydrogen and helium, which are computed in the same Jacobi iteration as the chemistry. Cooling from heavier elements (known as “metals” in astronomy) based on a set of lookup tables computed with the CLOUDY code [108] can also be included [109, 110].

Star Formation and Feedback

Star formation and feedback processes are modeled by simple heuristic methods based on the work of [111], which involves the identification of plausible site of star formation according to a set of criteria, e.g., dense gas with a short cooling time. The local star formation rate can be calculated by several methods, such as the density-dependent method based on Schmidt-Kennicutt relation [112]. The affected gas is converted to a star particle over a few dynamical times, and metals and thermal energy are injected into region surrounding the star particle accordingly. Simulations of single Pop III stars rather than ensembles are also utilized to model high-resolution star formation, which is calibrated by ab initio simulations of primordial star formation.

2.2 Halo Finding

In Λ CDM cosmology, dark matter (DM) halos form the basis of the gravitational potential in which galaxies form, and therefore the building blocks of universe. All of the analysis

in this work is based on statistics over all the DM halos in a single simulation volume. However, identifying halos in numerical simulation is far from a trivial task. Because simulated DM halos consist of discrete DM particles, the task of finding halos boils down to dividing dark matter halos into different dense groups.

There are over a dozen of packages available now specifically for this task (see Knebe et al. 2011 [113]). However, most of these codes share some common basic methods, which I will briefly review here.

2.2.1 Friends-of-friends Method

The friends-of-friends (FOF) method is the first kind of method proposed to address the halo-finding problem, which can be traced back to Davis et al. [114]. The idea is simple: attach any two particles to the same group if they are within a prespecified linking length, resulting in an interconnected group of particles that is considered a halo. Typically, the linking length is chosen in terms of a fraction b of the mean interparticle distance, usually in the range 0.15–0.2 [115].

While it seems straightforward and easy to implement, in practice this method has two main drawbacks:

- Setting a uniform linking length means that in high density regions, particles might have to link tens of thousands of neighbors whose distance is much smaller than the linking length, which is very inefficient. Although this disadvantage can be mitigated by adaptively adjusting the linking length at different densities, this approach involves calculating a density estimation which technically is not pure a FOF method anymore.
- Using a linking length as the only criterion to group particles can result in highly irregular halo shapes, having a lot of filaments. Consider an illustrative example: if two disjoint spherically symmetric halos are close enough so that the closest pair of

particles on the two halo surfaces are within linking length from each other, these two halos will be identified as one halo, which is obviously unphysical.

2.2.2 HOP Method

HOP method was proposed in Eisenstein & Hut [116]. The idea is to divide the particles into distinct sets such that particles in individual high-density regions (e.g. halos) are grouped together and left separate from those in other regions. In order to do that, we distinguish between nearby groups by assigning each particle to the group nucleus that it reaches by following in the direction of increasing density. This is done by calculating an estimate of the density at every particle position and then finding the highest density particle position among each particle and its $N_{\text{hop}} - 1$ nearest neighbors, i.e., finding the density peak. The value of N_{hop} is usually taken to be ~ 16 . Notice here that if the particle itself has the highest density among itself and its $N_{\text{hop}} - 1$ nearest neighbors, it will be the nucleus of its group. Since the maximum density must be a finite value, this loop is guaranteed to end in finite steps. At the end of the loop, each particle is linked to its densest nearest neighbor. Chains of particles are built by “hopping” (hence the name) from lower to higher density particles, and the chain terminates on a particle that is its own densest nearest neighbor.

There is usually no restriction on the chain otherwise, so its shape can often be very irregular, just as the case in FOF. Thus the last step is to merge geometrically adjacent chains into halos according to merging rules and threshold cutoffs, which is usually a multiple of the mean density. This way, the final object would have much smoother edge, and be a much more physically meaningful representation of a DM halo.

The density at each particle position is estimated by using a spherically symmetric cubic spline kernel [117] and radial positions of the $N_{\text{dens}} \sim 64$ nearest neighbors, giving unit weight to particles at zero distance from the given particle and zero weight to those at distances equal to the N_{dens} nearest neighbors.

2.2.3 Rockstar Method

The previous two methods are classic approaches and are the basis of many modern halo-finding packages. However, they have some common drawbacks. One is that since they only utilize the position space, it is not capable of identify substructure within individual DM halos, so-called subhalos. The other is that during major mergers, the density contrast alone is not enough to distinguish which particles belongs to which halo, so when two halos are close enough, the assignment of particles is virtually random in the overlap region.

However, both of these drawbacks can be overcome if we also utilize the velocity information and thus distinguish two clusters in space-velocity phase space. ROCKSTAR is an open source phase space based halo finder designed not only to overcome the aforementioned drawbacks, but also to maximize halo consistency across timesteps, and it is the halo finder used in this work. For the details of ROCKSTAR, please refer to its method paper [118].

The algorithm combines FOF and AMR:

- As a first step, it performs a rapid variant of the 3D position-space FOF to find overdense regions.
- Then for each 3D FOF group created in the first step, the algorithm proceeds to build a hierarchy of FOF subgroups in position-velocity phase space. Like AMR, deeper levels of subgroups have a tighter linking-length criterion in phase space, which means that deeper levels correspond to tighter isodensity contours around peaks in the phase-space density distribution. This enables us to easily distinguish substructures. The hierarchy ends at the deepest level of subgroups, at which a pre-specified minimum number of particles remains in the same group.
- The last step is to convert all phase-space FOF subgroups to halos, working from the deepest level bottom-up recursively. First in each of the subgroups at deepest level of the FOF hierarchy (centers at the local phase space density maxima), a seed halo

is generated. Then the algorithm recursively analyzes higher levels of the hierarchy and assigns particles to these seed halos, until some density cutoff limit is met. This final part of the ROCKSTAR algorithm is very similar to the last step of HOP.

CHAPTER 3

SIMULATION SETUP

3.1 Cosmology parameters

We use a comoving simulation volume of 1 Mpc^3 that has a 256^3 root grid resolution which gives a dark matter (DM) mass resolution of $1840 M_\odot$. This resolution enables us to resolve minihalos with at least 100 DM particles, allowing us to resolve $2 \times 10^5 M_\odot$ DM halos that can cool by H_2 [119]. We refine the grid on baryon overdensities of $3 \times 2^{-0.2l}$, where l is the AMR level, resulting in a super-Lagrangian behavior [120]. DM overdensity is refined to three, and local Jeans length is refined by at least 4 cells to avoid artificial fragmentation during gaseous collapse [121]. If any of the above criteria are met in a single cell, it is flagged for further spatial refinement. Maximum refinement level is set at $l = 12$, resulting in a maximal comoving spatial resolution of 1 pc. The adaptive particle-mesh solver has a source resolution of two cell widths of a given AMR grid. We stop the simulation at $z \sim 9$ to prevent any large-scale modes with $r \sim L_{\text{box}}/2$ from entering the non-linear growth regime. We write approximately 1000 outputs every 0.5 Myr.

The initial conditions were generated with MUSIC [122] at redshift $z = 130$. The cosmological parameters are adopted from the 2013 Planck results [123]: $\Omega_M = 0.3175$, $\Omega_\Lambda = 0.6825$, $\Omega_b = 0.049$, $h = 0.6711$, $\sigma_8 = 0.8344$, and $n = 0.9624$, where the variables have the usual definitions.

3.2 Radiative cooling

We use the nine-species (see Section 2.1.2) non-equilibrium chemistry model in Enzo [124, 125] that tracks atomic hydrogen and helium species, along with molecular hydrogen but not species containing deuterium. We spatially distinguish the metal ejecta from Pop III

and metal-enriched stars, and we obtain the cooling rates in the simulation from a tabulated cooling rate table that is calculated with CLOUDY [109]. This sophisticated photoionization solver includes all atomic species and many molecular species in a complex reaction network. We use a cooling rate table that is logarithmically spaced in four dimensions with a spacing Δ :

1. Density: 10^{-6} to 10^6 cm^{-3} , $\Delta = 0.25$ dex;
2. Temperature: 10 to 10^8 K , $\Delta = 0.1$ dex;
3. Electron fraction: 10^{-6} to 1, $\Delta = 0.25$ dex;
4. Metallicity: 10^{-6} to $1Z_{\odot}$, $\Delta = 1$ dex;

In the CLOUDY calculations, a CMB radiation spectrum was used as the input spectrum. In addition to these radiative cooling processes, we include a uniform radiation background that dissociates molecular hydrogen, which we describe next.

3.3 Molecular hydrogen dissociating background

A time-dependent Lyman-Werner (LW) optically thin radiation background is utilized in this simulation on which the LW radiation from point sources are added. LW flux from point sources dominates over the background within 3 kpc, dissociating H_2 and thus delaying Pop III star formation in nearby haloes [126, 127, 120]. We use the semi-analytical model of Wise & Abel [128], updated with the 7-year WMAP parameters and optical depth to Thomson scattering. The LW radiation intensity is plotted in Figure 3.1. For convenience, we fit the background evolution with function

$$\log J_{21}(z) = A + Bz + Cz^2 + Dz^3 + Ez^4 \quad (3.1)$$

where $(A, B, C, D, E) = (2.567, 0.4562, 0.02680, 5.882 \times 10^{-4}, -5.056 \times 10^{-6})$ and J_{21} is the specific intensity in units of $10^{-21} \text{ erg s}^{-1} \text{ cm}^{-2} \text{ Hz}^{-1} \text{ sr}^{-1}$. This fits the model data

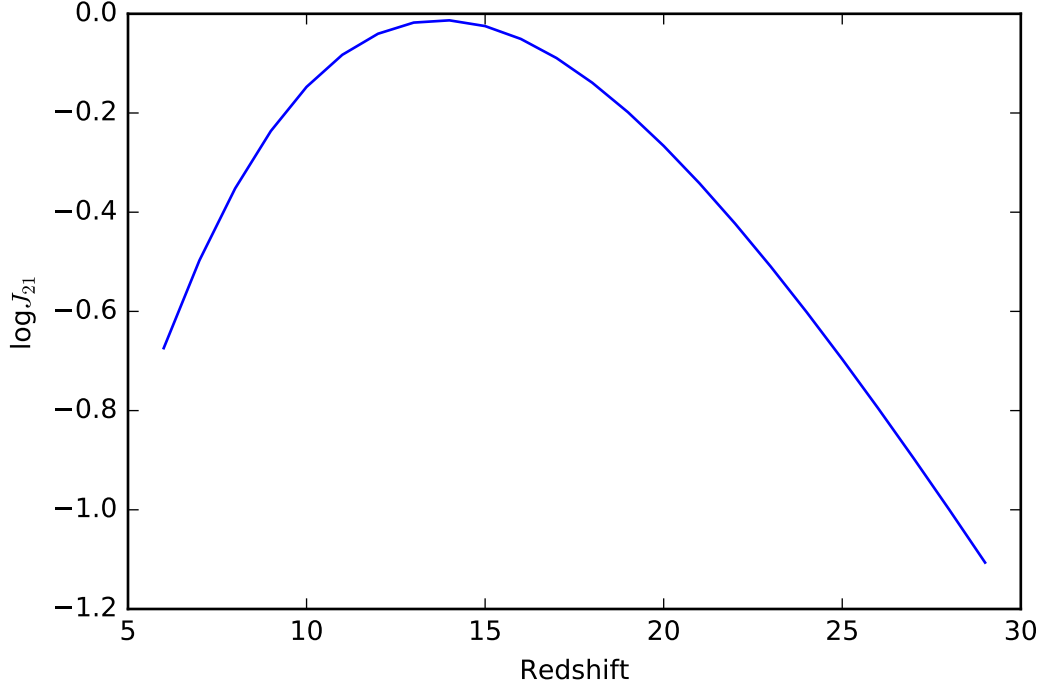


Figure 3.1: Time evolution of the Lyman-Werner background in unit of $J_{21} = 10^{-21} \text{erg s}^{-1} \text{cm}^{-2} \text{Hz}^{-1} \text{sr}^{-1}$, calculated with an updated version of the model in [128]

within 1 percent in $6 \leq z \leq 30$ and is consistent with J_{21} values in Trenti & Stiavelli [129].

This Lyman-Werner background radiation can be attenuated in dense, molecular hydrogen rich gas. Rather than performing radiative transfer on the 76 rotational and vibrational transition lines of H_2 , we approximate the absorption through a fitting function. We use an improved variant of the original self-shielding function by Draine & Bertoldi [130], which reads as

$$f_{\text{sh}} = \min \left[1, \left(\frac{N_{\text{H}_2}}{10^{14} \text{cm}^{-2}} \right)^{-3/4} \right], \quad (3.2)$$

where N_{H_2} is the H_2 column density between the intergalactic medium and some position in the simulation. These authors and later Wolcott-Green et al. [131] also included an improved treatment of line broadening and overlap that altered this power-law to become

$$f_{\text{sh}} = \frac{0.965}{(1 + x/b_5)^{1.1}} + \frac{0.035}{(1 + x)^{0.5}} \times \exp \left[-8.5 \times 10^{-4} (1 + x)^{0.5} \right]. \quad (3.3)$$

Here $x \equiv N_{\text{H}_2}/5 \times 10^{14} \text{ cm}^{-2}$, $b_5 \equiv b/10^5 \text{ cm s}^{-1}$, and b is the Doppler broadening parameter. For simulations, the difficulty lies in calculating the column density for each cell. There exist several approximations without resorting to ray tracing the domain. Most define a characteristic length scale L_{char} in which the local density is related to the column density,

$$N_{\text{H}_2} = n_{\text{H}_2} L_{\text{char}} \quad (3.4)$$

We select the Wolcott-Green et al. [131] best-fitting method that uses the ‘‘Sobolev-like’’ length for L_{char}

$$L_{\text{char}} \equiv L_{\text{Sob-like}} = \frac{\rho}{|\nabla \rho|} \quad (3.5)$$

and is spherically averaged and only considers values in the average with $d\rho/ds > 0$ so that only directions toward dense regions are not considered.

3.4 Star formation

Pop II and Pop III star formation (SF) are distinguished by total metallicity of the densest cell in the molecular cloud. Pop III stars are formed if $[Z/H] < -4$, and Pop II stars are formed otherwise.

3.4.1 Pop III Stars

The Pop III SF model are the same as Wise & Abel [132], in which each star particle represents a single star. A star particle forms when a cell meets all of the following requirements:

- a total gas number density of 10^6 cm^{-3} ,
- a converging gas flow ($\nabla \cdot \mathbf{v}_{\text{gas}} < 0$), and
- a molecular hydrogen fraction $f_{\text{H}_2} > 5 \times 10^{-4}$.

These requirements are typical for collapsing metal-free molecular clouds at $\sim 10 \text{ Myr}$ before the birth of a Pop III main-sequence star [133], [134], roughly when initial free-fall

Table 3.1: Fractional metal-free stellar endpoints for different characteristic masses

Endpoint	$M_{\text{char}} = 10M_{\odot}$	$M_{\text{char}} = 40M_{\odot}$	$M_{\text{char}} = 100M_{\odot}$
Black hole	14%	59%	64%
Type II supernova	68%	30%	1%
Pair-instability supernova	1%	11%	35%

Note: The $M_{\text{char}} = 10M_{\odot}$ does not add to unity because there exist stars that are not massive enough to produce supernovae but will die in planetary nebulae.

phase ends. The fragmentation mass scale is characterized by the minimum temperature at this stage [135]. The molecular hydrogen fraction requirement effectively constrains star formation to cooling molecular clouds, in which the H_2 formation rate is significantly larger than the dissociation rate from a Lyman-Werner radiation field.

The Pop III stellar masses are randomly sampled from an IMF

$$f(\log M)dM = M^{-1.4} \exp \left[- \left(\frac{M_{\text{char}}}{M} \right)^{1.6} \right] dM \quad (3.6)$$

that behaves as a power-law IMF at $M > M_{\text{char}}$ and is cutoff exponentially below that mass [136]. We can integrate this IMF over all possible masses ($0.1 - 500M_{\odot}$) to determine the fraction of stars with particular endpoints: a Type II supernova, a direct-collapse stellar-mass black hole, or a pair-instability supernovae (see Section 1.2.2. We show the expected fractional endpoints in Table 3.1 for different characteristic masses $M_{\text{char}} = 10, 40,$ and $100 M_{\odot}$. One can see that for a top-heavy IMF, over half of the Pop III stars produce black holes after their death. In this simulation we choose $M_{\text{char}} = 40M_{\odot}$. Latest results of Pop III stars formation simulation shows that choosing M_{char} this way is more consistent [137, 138, 139, 140].

If multiple cells meet the star particle formation criteria within 1 pc, we form one Pop III star particle with the center of mass of these flagged cells to ensure that one massive star is created per metal metal-free molecular cloud. After the star particle forms and its mass is determined, an equal mass of gas is removed from the grid in a sphere that contains twice the stellar mass and is centered on the star particle. At this stage of collapse, a sphere

enclosing $200M_{\odot}$ has a radius of 1–2 pc and has about 200 cells. The velocity of the star particle is set as the mass-weighted velocity of the gas contained in the sphere.

3.4.2 Pop II stars

The prescription of Pop II star formation is similar to the one for Pop III star but without the requirement of minimum H_2 fraction. This requirement is not necessary because metal-enriched gas can cool efficiently even in a strong UV radiation field [141]. In addition, we restrict star formation in cold gas with temperature $T < 1000K$. Another difference is that Pop II star particles represent a star cluster of some total mass and assumed Salpeter IMF instead of a single star particle that represents a Pop III star whose mass is drawn from an IMF (Equation 3.6).

When a cell meets these criteria, the prescription searched outward with increasing radius for the boundary of the molecular cloud from the most dense cell. The molecular cloud here is defined as a sphere with a dynamical time $t_{\text{dyn}} = 3Myr$, which corresponds to an average density $\bar{\rho}_{\text{MC}} \simeq 500\mu \text{ cm}^{-3}$, where μ is the mean molecular weight. The radius of the molecular cloud defined as such is typically 6 pc for the smallest ones and include 2500 cells, increasing as $M_{\text{MC}}^{1/3}$. Once the radius is determined, a fraction $c_{\star} = 0.07f_{\text{cold}}$ of the cold gas with temperature $T < 1000 \text{ K}$ inside the sphere is converted to a star particle with mass $m_{\star} = c_{\star}(4\pi/3)\bar{\rho}_{\text{MC}}R_{\text{MC}}^3$. After the star particle is created, we replace the sphere with a uniform density $\rho_{\text{MC}} = (1 - c_{\star})/(Gt_{\text{dyn}}^2)$ and temperature $T = 10^4 \text{ K}$, which is approximately the environment of initial stages of an H II region.

3.5 Stellar feedback

After a star is created, we take into account its radiative feedback which ionizes neutral hydrogen. The radiation field is evolved with adaptive ray tracing [142, 143] based on the HEALPix framework [144] and is self-consistently coupled to the hydrodynamics. Each star is considered as a point source of radiation with a spectrum of energy that is sampled

by three energy groups:

1. Hydrogen-only ionizing photons: $E_{\text{ph}} = 28$ eV for Pop III stars and 21.6 eV for Pop II stars;
2. Neutral helium ionizing photons: $E_{\text{ph}} = 30$ eV;
3. Singly-ionized helium ionizing photons: $E_{\text{ph}} = 60$ eV.

The luminosity of the star is equally split into 48 rays initially in each energy group, and each of them adaptively split into 4 child rays as they propagate into a high resolution AMR grid and the solid angle of the ray $\theta = 4\pi/(12 \times 4^L)$ is larger than 1/3 of the cell area, where L is the HEALPix level. The maximum HEALPix level is limited to 13, which is equivalent to 8.05×10^8 rays per source. The H₂ dissociating radiation is modeled as optically-thin, inverse-square profile, centered on all Pop II and Pop III star particles, and is added to the radiation background that was described in Section 3.3.

In addition to photo-ionization and photo-heating, the simulation in this work considers momentum transfer from (continuum) ionizing radiation to the absorbing gas. The momentum of absorbed ionizing radiation

$$d\mathbf{P}_{\text{rp}} = \frac{dP E_{\text{ph}} \hat{\mathbf{r}}}{c} \quad (3.7)$$

is transferred to the absorbing medium, where dP is the number of photons absorbed, E_{ph} is the photon energy, and $\hat{\mathbf{r}}$ is the normal direction of the radiation. The gas that absorbs this momentum acquires an acceleration

$$da_{\text{ap}} = \frac{d\mathbf{p}_{\text{rp}}}{dt \rho V_{\text{cell}}} \quad (3.8)$$

per unit mass, where ρ is the gas density, dt is the radiative transfer timestep, and V_{cell} is the cell volume.

3.5.1 Pop III stellar feedback

Radiative feedback

The lifetime of Pop III stars and their mass-dependent hydrogen ionizing and LW photon luminosities is adopted from Schaerer [145]. They die as Type II SNe if $11M_{\odot} \leq M_{\star} \leq 40M_{\odot}$, or as PISNe if $140M_{\odot} \leq M_{\star} \leq 260M_{\odot}$ (see section 1.2.2). For Type II SNe between 11–20 M_{\odot} , we use an explosion energy of 10^{51} erg and a linear fit to the metal ejecta mass [146]

$$M_Z/M_{\odot} = 0.1077 + 0.3383 \times (M_{\star}/M_{\odot} - 11). \quad (3.9)$$

The corresponding metal yield fraction is

$$y = 0.3383 - 3.614M_{\star}^{-1}. \quad (3.10)$$

We model the SNe of stars with $20M_{\odot} \leq M_{\star} \leq 40M_{\odot}$ as hypernova with energies and ejecta masses ($y \sim 0.15 - 0.2$) also taken from Nomoto et al., linearly interpolating their results to M_{\star} . For PISNe, we use the explosion energy from Herger & Woosley [147], where we fit the following function to their models,

$$E_{\text{PISN}} = 10^{51} \times [5.0 + 1.304(M_{\text{He}}/M_{\odot} - 64)] \text{ erg}, \quad (3.11)$$

where $M_{\text{He}} = 13/24 \times (M_{\star} - 20)M_{\odot}$ is the metal ejecta (helium core) mass. If the stellar mass is outside there ranges, then an inert, collisionless black hole (BH) particle is created.

Mechanical feedback

Besides radiation, SNe also generates a blastwave that eject stellar material into space around it. The blastwave is modeled by injecting the explosion energy and ejecta mass into a sphere of 10 pc, smoothed at its surface to improve numerical stability [132]. We resolve the blastwave with several cells across at its initialization. The thermal energy is converted

into kinetic energy and agrees with the Sedov-Taylor solution [148].

3.5.2 Pop II stellar feedback

We set Pop II star particles to emit 6000 hydrogen ionizing photons per stellar baryon averaged over their lifetime, or equivalently 1.12×10^{46} ionizing photons $\text{s}^{-1}M_{\odot}^{-1}$ [149]. The star particles live for 20 Myr, the maximum lifetime of an OB star. These stars generate most of the ionizing radiation and SNe feed back in stellar clusters, so we ignore any feedback from lower mass stars. Assuming a constant luminosity may underestimate the impact of the radiative feedback because given an IMF, the total luminosity of a cluster is maximal at early times when thermal and radiation pressure forces are greatest, i.e. the edge of H II region is still near the massive stars.

For SN feedback, these stars generate $6.8 \times 10^{48} \text{erg s}^{-1}M_{\odot}^{-1}$ after living for 4 Myr, which is injected into spheres with a radius of 10 pc. if the resolution of the grid is less than 10/3 pc, we distribute the energy into a 3^3 cubic grid region surrounding the star particle. Star particles also return ejected material with mass

$$\Delta m_{\text{ej}} = \frac{0.25 \Delta t M_{\star}}{t_0 - 4 \text{ Myr}}, \quad \text{when } (4 \text{ Myr} < t - t_{\text{birth}} < t_0) \quad (3.12)$$

back to the finest grid at each timestep. $t_0 = 20$ Myr is the lifetime of the star particle. The ejected gas has solar metallicity $Z = 0.02$, giving a total metal yield $y = 0.0005$.

CHAPTER 4

ORBITAL MECHANICS

4.1 Orbital analysis

The main goal of this work is to investigate the orbital dynamics of a large set of seed black holes spread out in many first galaxies, which is crucial to their growth and merger rate. Although we have the exact location and velocity of each black hole at every timestep, the time difference between these snapshots are not small enough to trace out a smooth orbit of each black hole, which requires too much computational resources.

We instead approximate the potential field of their host halos in analytical form, and use the position and velocity data of each black hole at each timestep to calculate their approximated orbits, characterized by semi-major axis (*sma*) and eccentricity (*ecc*) given the potential stays the same at each snapshot. This way we can see how the orbits of these BHs change over time. Two approximation methods, point-mass potential and spherically-averaged potential were carried out, described in detail below in this section. The results of these two methods are presented in next chapter.

4.1.1 Point mass approximation

This is the first and simplest approximation. We assume the total mass of the halo is concentrated at one point, its center. Therefore, given the position and velocity of BH particle, it is easy to calculate its orbit. Let \vec{r} be the position vector relative to the center of halo, \vec{v} be the velocity vector relative to the velocity of halo, and M be the mass of the halo. Then the semi-major axis *sma* is given by

$$sma = \left(\frac{2}{r} - \frac{v^2}{GM} \right)^{-1} \quad (4.1)$$

where $r = |\vec{r}|$, and $v = |\vec{v}|$. Notice here we only consider the BHs bounded by the halo potential, so the orbit is supposed to be elliptic. For hyperbola or parabola the equations are different. Eccentricity ecc is given by magnitude of eccentricity vector, \vec{e} , which is in turn given by

$$\vec{e} = \left(\frac{v^2}{GM} - \frac{1}{r} \right) \vec{r} - \frac{\vec{r} \cdot \vec{v}}{GM} \vec{v} \quad (4.2)$$

4.1.2 Using the simulated gravitational potential

The point mass approximation is likely a bad approximation because it over-simplifies the extended and clumpy mass distribution inside dark matter halos. Fortunately, Enzo can output the gravitational potential (see Equation 2.8 and Section 2.1.2, which can be used in the orbital analysis.

The contribution from collisionless matter is calculated by depositing the dark matter, star, and black hole particle masses onto the adaptive mesh with a second-order cloud-in-cell (CIC) interpolation [106] to formulate the cumulative density field $\rho_{\text{DM}} + \rho_{\text{stars}}$. During the interpolation, the particles are integrated to the next half timestep so that the density field is time centered. The baryon density field ρ_{gas} is also integrated so that it is time centered as well.

To compute the gravitational potential ϕ on the uniform root grid, a Fast Fourier Transfer is used by multiplying the Fourier transfer of the density field $\tilde{\rho}(k)$ by the finite difference formulation of a Greens function kernel of $-k^{-2}$ [106]:

$$G(\mathbf{k}) = -\frac{\Delta x}{2[\sin(k_x \Delta x/2)^2 + \sin(k_y \Delta y/2)^2 + \sin(k_z \Delta z/2)^2]}, \quad (4.3)$$

where $k^2 = k_x^2 + k_y^2 + k_z^2$ is the wavenumber in Fourier space and $\Delta[xyz]$ is the cell width in each Cartesian direction. The potential is then calculated by taking the inverse FFT of $\tilde{\phi}(k) = G(k)\tilde{\rho}(k)$. The potential on the AMR grids are then calculated using a multigrid method, ensuring that the boundary conditions are consistent between neighboring grids.

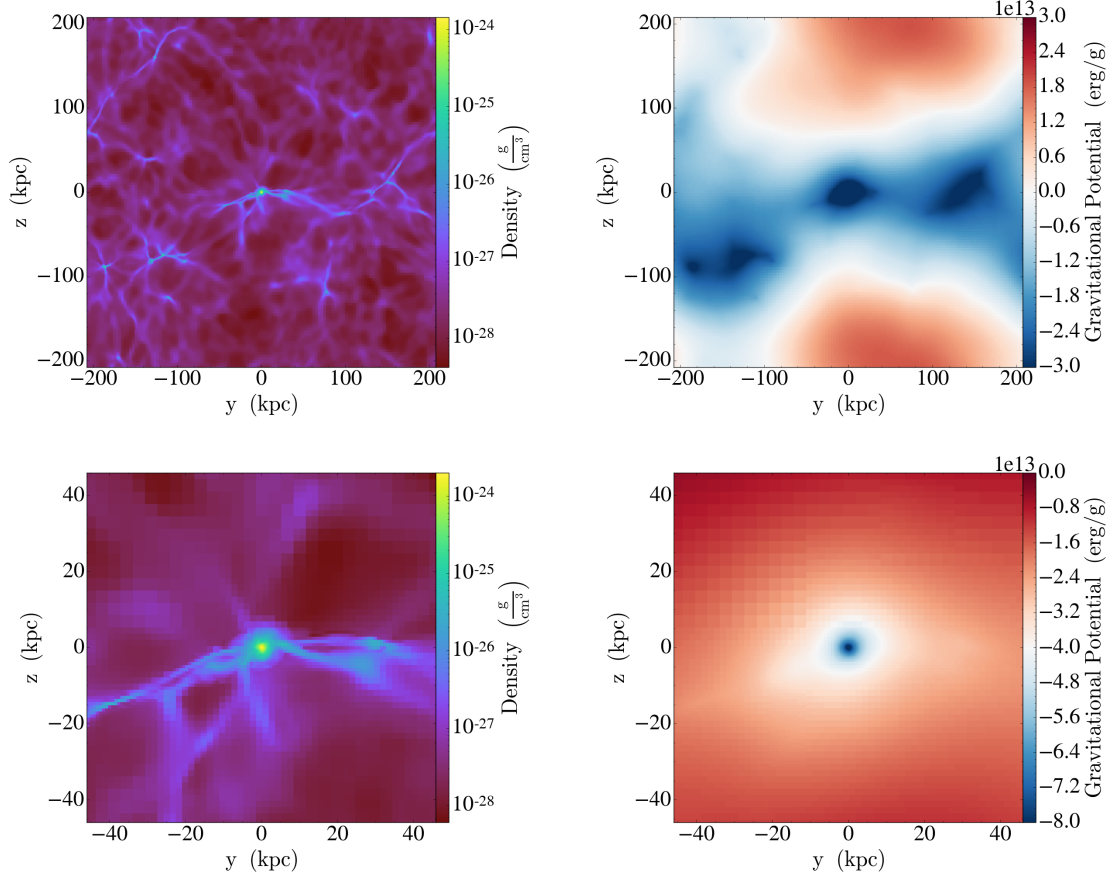


Figure 4.1: Slices of gas density (left) and gravitational potential (right) of the simulation at $z = 10$, focused on a halo with a halo mass $M_{\text{vir}} = 1.2 \times 10^9 M_{\odot}$ and virial radius $r_{\text{vir}} = 4.59$ kpc. The top panels show the entire simulation domain, whereas we restrict the field of view to $20 r_{\text{vir}}$ in the bottom panels. Note that the colorbar ranges are different for the gravitational potentials, which is approximately spherical near the halo.

We show slices of the gas density and calculated gravitational potential in Figure 4.1 of a sample halo with a virial mass $M_{\text{vir}} = 1.2 \times 10^9 M_{\odot}$ and a virial radius $r_{\text{vir}} = 4.59$ kpc at $z = 10$. These panels show the entire simulation domain in the top panels and the halo and its neighborhood in the bottom panels. In the former, the gravitational potential is smooth and follows the cosmological large-scale structure in the simulation. However, it becomes more spherical near and inside the halo. Thus, we will consider a spherically-average potential for our black hole orbital analysis in each halo.

From this global potential, we can extract the potential $\phi(r, \theta, \varphi)$ inside the halo, and

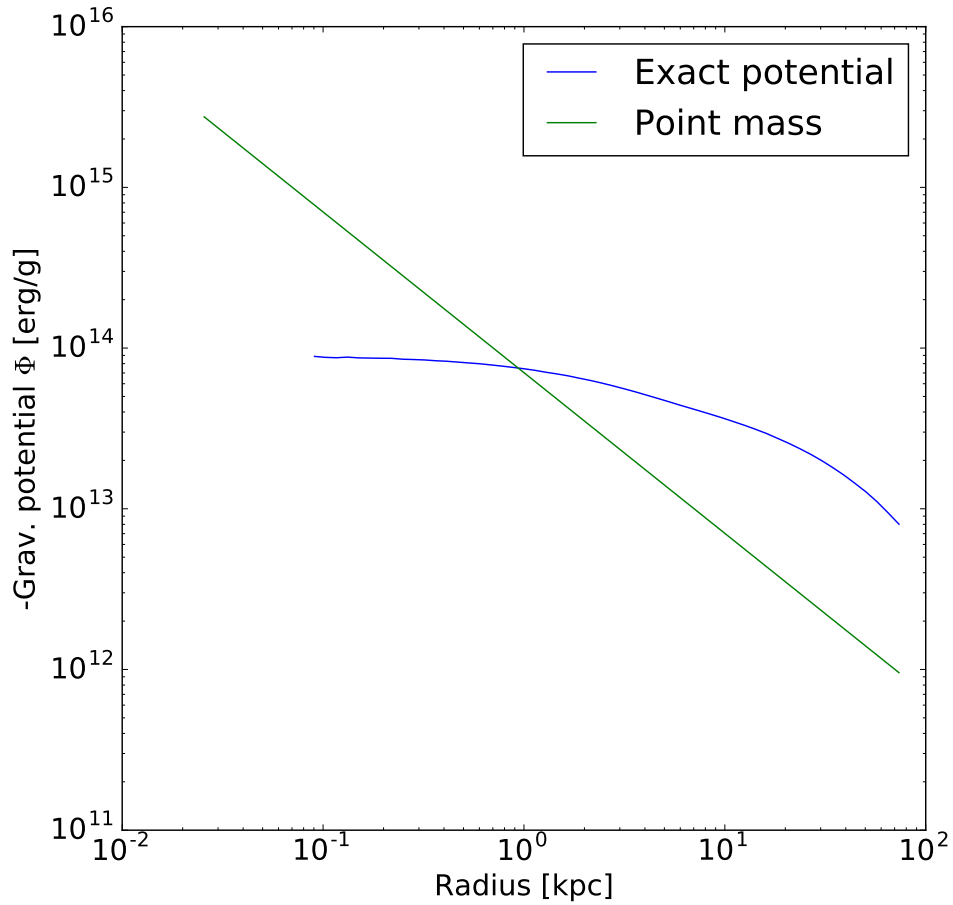


Figure 4.2: A comparison of the gravitational potentials of the same halo in Figure 4.1, using point mass approximation (green) and the potential calculated in Enzo (blue). The calculated potential is much flatter inside the halo and is more extended outside of it, which should result in more accurate black hole orbital calculations.

integrate it over θ and φ then divide it by 4π to obtain the spherically-averaged potential $\psi(r)$. Using this direct measure is a much better approximation than the point mass because of the extended mass distribution inside the halo, which we depict the differences between the two approaches in Figure 4.2. In this comparison, we show the gravitational potential in the same halo as Figure 4.1. Here one can see the gravitational potential having more of a core instead of a cusp in the central regions of the halo. In addition, the potential is much more extended than the point mass approximation, as expected. By enforcing spherical

symmetry, we can have an analytical equation to solve for *sma* and *ecc*. In this work $\psi(r)$ is obtained through numerical integration.

Particles in spherically symmetric potential have constant angular velocity, which means the particle moves in a plane, the **orbital plane**. Therefore we can use plane polar coordinates (r, θ) to describe the position of BHs, where r is the distance to halo center, and θ is the azimuthal angle in the orbital plane. We can then write the specific Lagrangian as

$$\mathcal{L} = \frac{1}{2}(\dot{r}^2 + (r\dot{\theta})^2) - \psi(r) \quad (4.4)$$

The equations of motion are

$$\frac{d}{dt} \frac{\partial \mathcal{L}}{\partial \dot{r}} - \frac{\partial \mathcal{L}}{\partial r} = \ddot{r} - r\dot{\theta}^2 + \frac{d\psi}{dr} = 0 \quad (4.5)$$

$$\frac{d}{dt} \frac{\partial \mathcal{L}}{\partial \dot{\theta}} - \frac{\partial \mathcal{L}}{\partial \theta} = \frac{d}{dt}(r^2\dot{\theta}) = 0 \quad (4.6)$$

The second equation of motion implies that

$$r^2\dot{\theta} = \text{constant} \equiv L \quad (4.7)$$

which is just the result of conservation of angular velocity (or specific angular momentum).

With equation 4.7, we can make the following substitution

$$\frac{d}{dt} = \frac{L}{r^2} \frac{d}{d\theta} \quad (4.8)$$

equation 4.5 becomes

$$\frac{L^2}{r^2} \frac{d}{d\theta} \left(\frac{1}{r^2} \frac{dr}{d\theta} \right) - \frac{L^2}{r^3} = -\frac{d\psi}{dr} \quad (4.9)$$

By making a change in variables $u \equiv 1/r$, this expression can be further simplified to

$$\frac{d^2u}{d\theta^2} + u = \frac{1}{L^2u^2} \frac{d\psi(1/u)}{dr} \quad (4.10)$$

In general the solution of this equation must be obtained numerically, and are of two types: along unbound orbits $r \rightarrow \infty$ and hence $u \rightarrow 0$, while on bound orbits, r and u oscillate between finite limits. In order to find these two limit values, we can multiply 4.10 by $du/d\theta$ and integrate over θ to obtain another conservation law

$$\left(\frac{du}{d\theta}\right)^2 + \frac{2\psi}{L^2} + u^2 = \text{constant} \equiv \frac{2E}{L^2} \quad (4.11)$$

For bound orbits, at two limit values of u (hence r), we have $du/d\theta = 0$, thus equation 4.11 becomes

$$u^2 + \frac{2(\psi(1/u) - E)}{L^2} = 0 \quad (4.12)$$

Normally we have two roots u_1 and u_2 between which the star oscillates radially as it revolves in θ . The orbit is confined between, inner radius $r_p = 1/u_1$, a.k.a. the **pericenter** distance, and outer radius $r_a = 1/u_2$, a.k.a. **apocenter** distance. Of course for a circular orbit these two radii are the same. In general these two roots must be solved numerically. After we have these two roots, we can easily calculate *sm* and *ecc* as $sm = (r_a + r_p)/2$ and $ecc = (r_a - r_p)/(r_a + r_p)$.

4.2 Dynamical Friction

The black holes in this simulation are inert DM particles, which interact with other particles only through gravity. Dynamic friction will be the main factor that affect the orbit properties of BH particles.

Assuming the density profile of the host halo is a singular isothermal sphere (SIS):

$$\rho(r) = \frac{v_c^2}{4\pi G r^2} \quad (4.13)$$

where, σ is the velocity dispersion, $v_c = \sqrt{2}\sigma$ is the constant circular speed, the dynamic friction force on the black hole is given by

$$F = \frac{4\pi G^2 M^2 \rho(r) \ln \Lambda}{v_c^2} \left[\text{erf}(X) - \frac{2X}{\sqrt{\pi}} e^{-X^2} \right] = 0.428 \frac{GM^2}{r^2} \ln \Lambda \quad (4.14)$$

where $X = v_c/(\sqrt{2}\sigma) = 1$ for SIS, Λ is the ratio of maximum impact parameter over 90 degree deflection radius, and M is the mass of black hole.

This force is tangential to the trajectory of the BH and directed opposite to the velocity of the black hole, causing it to lose angular momentum L at a rate

$$\frac{dL}{dt} = -Fr \simeq -0.428 \ln \Lambda \frac{GM^2}{r} \quad (4.15)$$

Assuming the black hole orbit is circular without dynamic friction, then with friction, the black hole continues to orbit at speed v_c as it spirals inward, with angular momentum $L = Mrv_c$ at radius r . Thus we have

$$\frac{dL}{dt} = \frac{\partial L}{\partial r} \frac{dr}{dt} + \frac{\partial L}{\partial v_c} \frac{dv_c}{dt} = Mv_c \frac{dr}{dt} \quad (4.16)$$

Combine the last two equations, we have

$$r \frac{dr}{dt} = -0.428 \ln \Lambda \frac{GM}{v_c} = -0.302 \ln \Lambda \frac{GM}{\sigma} \quad (4.17)$$

$$\Rightarrow t_{\text{fric}} = \frac{1.65}{\ln \Lambda} \frac{r_i^2 \sigma}{GM} = \frac{1.17}{\ln \Lambda} \frac{\mathcal{M}(r)}{M} t_{\text{cross}} \quad (4.18)$$

where r_i is the initial radius, $\mathcal{M}(r) = v_c^2 r / G$ is the mass of the host galaxy contained within radius r , and $t_{\text{cross}} = r_i / v_c$ is the time for black hole to trespass the diameter of

orbit circle with the same orbit velocity. The last equation gives the time needed for a BH particle whose orbit is nearly circular to sink to the center of halo with a SIS density profile. However, this result is approximately correct even for mass distributions other than SIS.

Now, if we loosen the restriction of nearly circular orbit, we can still use Equation 4.17 to roughly estimate t_{fric} for BHs with elliptical orbits at pericenter and apocenter, since only at these two points the velocity is perpendicular to the radial vector, satisfying the requirement of circular orbit. At these two points,

$$\mathcal{M}(r)|_{r_a, r_p} = M_{\text{vir}} \left(\frac{r}{r_{\text{vir}}} \right) = M_{\text{vir}} \left(\frac{sma}{r_{\text{vir}}} \right) (1 \pm ecc) \quad (4.19)$$

Thus the maximum and minimum value of t_{fric} is given by

$$t_{\text{fric}}|_{\text{max, min}} = \frac{1.17}{\ln \Lambda} \frac{M_{\text{vir}}}{M_{\text{bh}}} \left(\frac{sma}{r_{\text{vir}}} \right) (1 \pm ecc) t_{\text{cross}} \quad (4.20)$$

For a typical stellar mass seed BHs in a minihalo of $10^6 M_{\odot}$, $M_{\text{vir}}/M_{\text{bh}} \sim 10^6$. If $ecc = 0.95$, $sma = 0.1 r_{\text{vir}}$, and $t_{\text{cross}} = 10$ Myr, $t_{\text{fric, min}} = 50$ Gyr, longer than the age of universe.

The above calculation only considers collisionless matter as the source of dynamical friction (DF). It has been shown that collisional matter, such as gas, has much stronger (about 4 times) DF force when the object velocity is comparable to the local sound speed [150]. However, recent hydrodynamical simulations of accreting BHs suggest that the DF force from the surrounding gas medium can be greatly reduced due to BH radiative feedback that causes the ambient gas density to drop [151].

CHAPTER 5

RESULTS

As mentioned in chapter 3, BH particles are created as DM particle in the simulation after the death of Pop III stars with masses outside supernove ranges. After we finished the simulation, we extract all BH particles and Pop III star particles (which depending on its mass could form a BH after death) at each time step accordingly, and analyze their properties.

5.1 Formation of stellar-mass black holes

First we count the total number of BHs contained by DM haloes at each time step, and plot it in Figure 5.1.

We can see that the first Pop III star whose remnant is a black hole forms at $z = 25$, when the universe was only 130 Myr old. After $z = 18$, the number of black hole remnants steadily increase with time, and tops just above 700 at $z \sim 9$. At $z > 10$, there are two very short intervals when the number of black holes drops by about 150. Since we only count black holes that exist inside halos, these dips are caused by black holes wandering outside of the halos, only to be reincorporated into the halos as they merge to form larger halos.

The endpoints in simulation depend on the stellar mass, which are randomly drawn from the Pop III initial mass function (IMF). However because the IMF is thought to be top-heavy, there is a large probability that a large fraction (see table 3.1 of Pop III stellar remnants are black holes. Refer back to the Simualtion setup chapter (Equation 3.6 for the function form of it. The randomness of stellar masses of Pop III stars may also affect when the first black hole forms, but the Δz should not be more than a few redshift.

This simulation has a volume of 1 comoving Mpc³. The early evolution of the number of stellar-mass black holes at $z > 20$ would be different if the simulation volume were

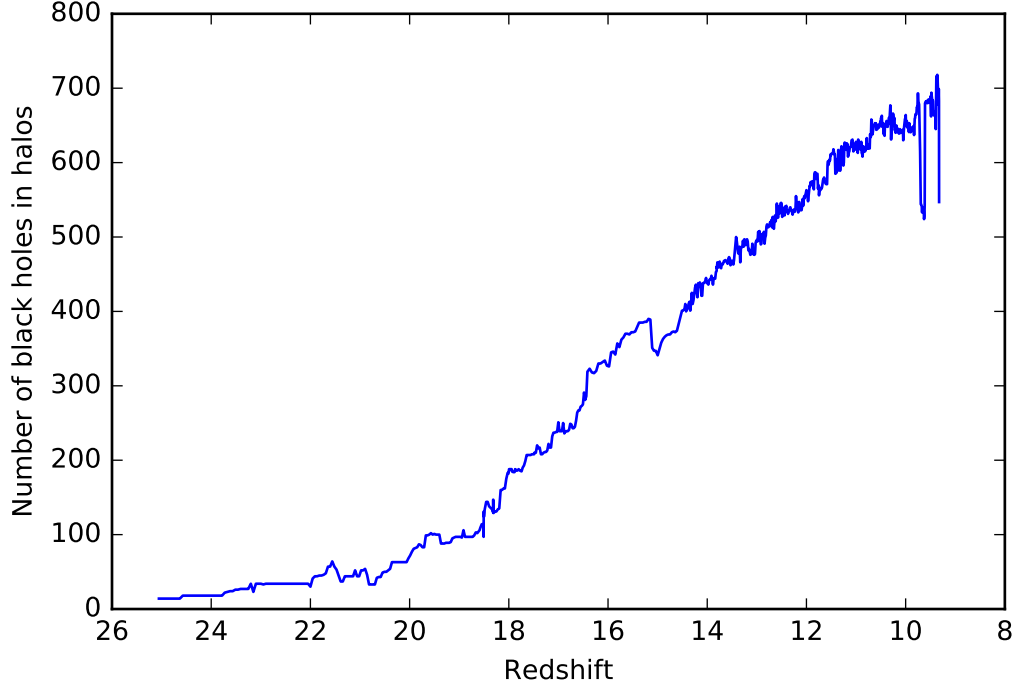


Figure 5.1: The total number of black hole remnants from Pop III stars that exist inside of dark matter halos in the simulation. After $z = 18$, it steadily rises as the Pop III star formation rate plateaus. The dips in the evolution correspond to black holes temporarily being ejected from their host halos during mergers.

larger. However, it converges to analytical expectations from Press-Schetcher formalism [72, 152],

$$N(M)dM = \frac{1}{\sqrt{\pi}} \left(1 + \frac{n}{3}\right) \frac{\bar{\rho}}{M^2} \left(\frac{M}{M^*}\right)^{(n+3)/6} \exp\left(-\left(\frac{M}{M^*}\right)^{(n+3)/3}\right) dM \quad (5.1)$$

Equation 5.1 predicts the number of objects between mass between M and $M + dM$, where $\bar{\rho}$ is the mean (baryonic and dark) matter density of the universe, n is the index of the power spectrum of the fluctuations in the early universe $P(k) \propto k^n$, and M^* is critical mass (see Equation 1.7, above which structures will form.

Since these black holes are Pop III star remnants, its number is directly tied to the Pop III star formation rate density, which has been shown to be roughly constant in the range $z = 6 - 20$ at a value of $\dot{M}_{*,3} \simeq 3 \times 10^{-5} M_{\odot} \text{ yr}^{-1} \text{ cMpc}^{-3}$ [153, 90], where the lower

case “c” indicates comoving units.

Now we inspect mass distribution of all halos v.s. mass distribution of halos that host BHs at four redshifts: $z = 9.33, 9.94, 10.69, 12.63$ (Figure 5.2). The number of black holes in these four snapshots all surpass 500, providing a good statistical sample. We can see that the total halo mass distribution is almost the same across the four redshifts, all peak at about $10^5 M_\odot$, although the number of halos have been increasing, from 2628 to 3511. For halos with BHs, the mass distribution changed slightly more but still are roughly the same, peaking at a little over $10^6 M_\odot$. On the other hand, the number of halos with BHs stays roughly the same: 116, 114, 117, 110. This invariance most likely occurs because Pop III BH remnants form in minihalos at a constant rate but then merge into larger halos as time progresses. Unlike the total distribution, the mass distributions of halos with BHs changes slightly more across all four snapshots, with steeper slope at lower mass end decreasing drastically under $10^6 M_\odot$. This is consistent with Pop III star formation theory that most Pop III stars form in minihalos with masses around $10^6 M_\odot$ (see Section 1.2.1). Halos with higher masses have steeper potential and thus are more capable of capturing Pop III stars, resulting in shallower slopes on higher mass end.

We further investigate the average number of BHs in halos in each bin of masses at the same four redshifts, shown in Figure 5.3. Here we can see that more massive halos tend to host more black holes because have deeper potential well which makes forming and capturing Pop III stars (hence black holes) easier. The rightmost bin of three higher redshifts seems unusually high, corresponding to a single halo with mass over $10^8 M_\odot$. We believe this seemingly abnormality can be removed if the simulation volume is larger so that we can have more massive halos that contain BHs.

The population of ~ 700 black holes gives us a good statistical sample in which we can calculate the orbital properties and their evolution over time. The biggest question is whether they can sink to the center of their host halos through dynamical friction or do they stay in orbits far away from the center. This is a key question in order to estimate the merger

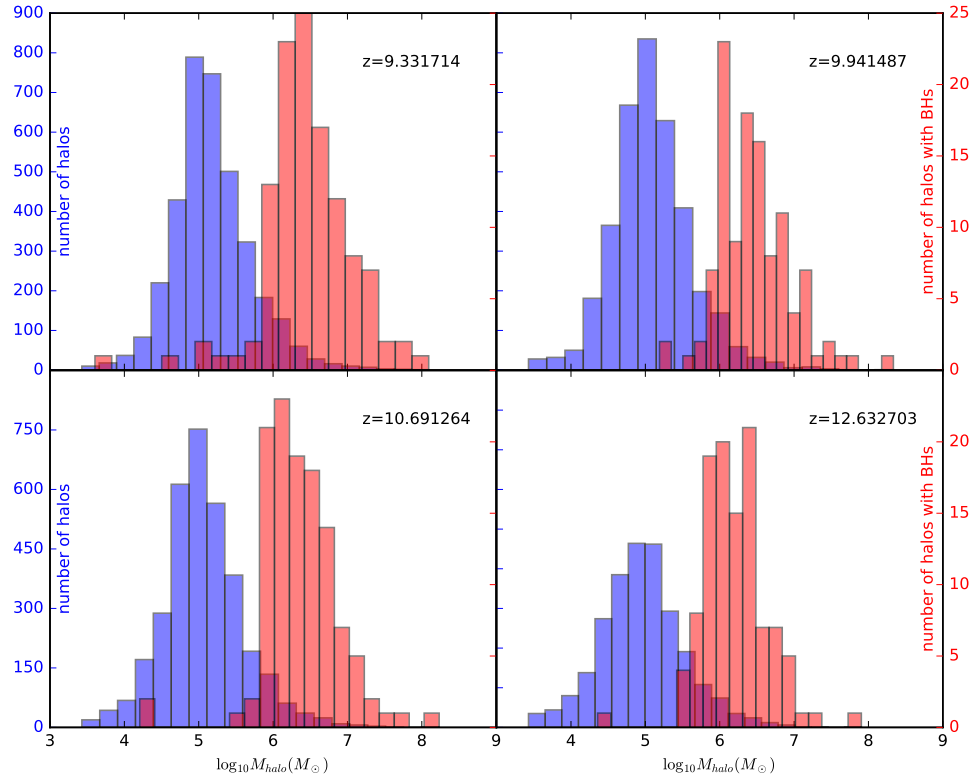


Figure 5.2: This figure shows the whole halo mass distribution and mass distribution of halos hosting BHs at four selected redshifts. The blue histograms correspond to all halos, and red correspond to halos with BHs. The blue patches are scaled to left y-axis with blue ticks, red patches are scaled to right y-axis with red ticks

rate and possible growth of central black holes before the dawn of galaxy formation.

5.2 Distribution of black holes within the first galaxies

We are interested in the spatial distribution of black holes that are Pop III remnants to inform us about the possible mergers of these stellar-mass compact objects in the first galaxies. From the position data of the BHs and the center of their their host halos, we can calculate the distance between each black hole and the center of its host halo. Since halo size varies in several orders of magnitude, we scale the distance by the virial radius (r_{vir}) of the corresponding halos.

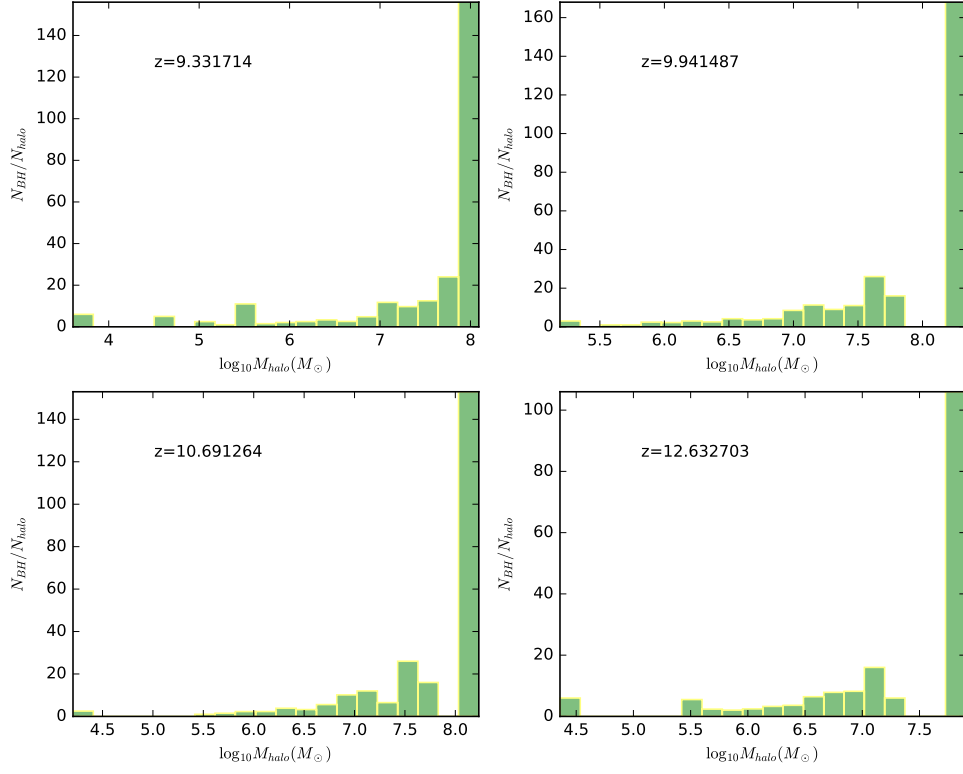


Figure 5.3: Average number of black holes per halo in corresponding mass range

First we look at the fraction of black holes that are within 10% of the virial radius of the host halo as a function of time (5.4 upper panel). Before $z \sim 18$, the fraction widely varies between 30% and unity. The reason is that, first, the number of black holes is relatively small at early stages, less than 150 as we can see from Figure 5.1; second, since the structures form in a bottom-up fashion (see section 1.2.1, halo shape changes relatively quickly and halo mergers occurs more frequently. Thus the center of host halos fluctuate a lot. Even at $z \sim 15$, we can still see that a major merger occurs and causes a drop in the fraction by 15% as the progenitor halos and their black holes' orbits are disrupted. After that the fraction stabilizes to approximately 50% until $z \sim 15$, dropping to 40% afterwards as more black holes form. The variations subside as they are incorporated into larger halos, less subject to disruption in major mergers.

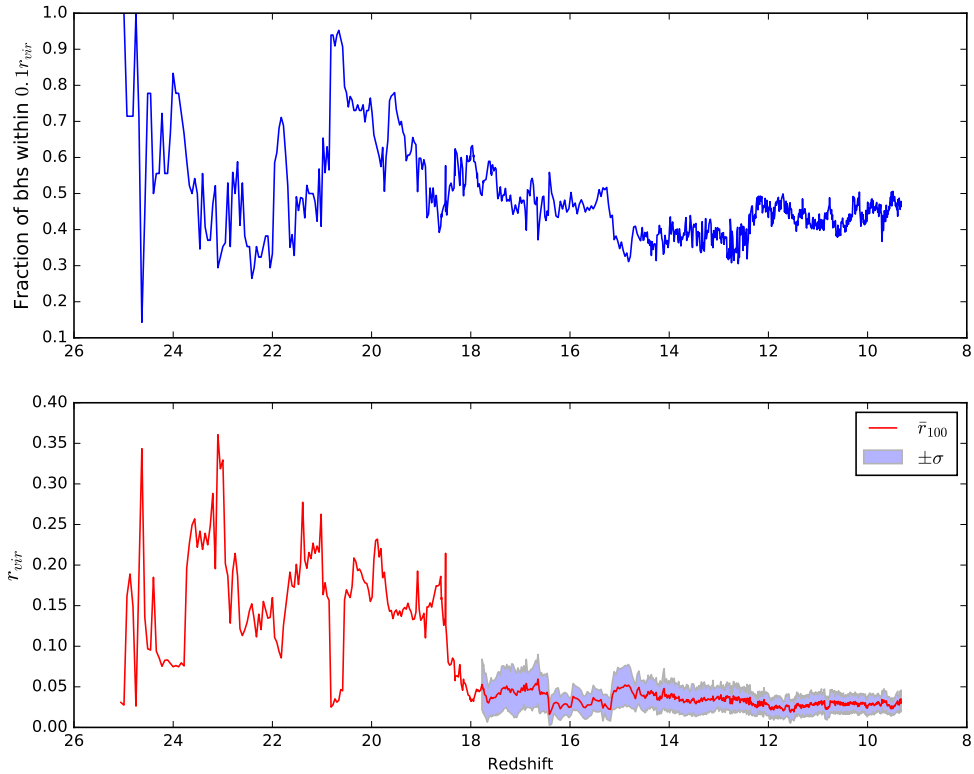


Figure 5.4: The time evolution of radial distribution of black holes. The upper panel shows the fraction of black holes that are within $0.1r_{vir}$ (virial radius of host halo). The lower panel shows the average radial distance of the 100 black holes that are closest to the halo center.

We now restrict our initial analysis on the radial distribution to the 100 black holes that are closest to their host halo center at each time step. Before $z \sim 18$, we see that the average fluctuates between 3% and 35% for the same reason as in the upper panel. Besides there are only a little over 100 black holes in the simulation before this time, so the average is influenced by black holes that exist in the outskirts of the halo. However after this time, the sample is now restricted to the innermost black holes. The average radial distance dramatically drops to 2-5% of the virial radius with a standard deviations on the order of a few percent. The major merger at $z \simeq 15$ also increases the average radial distance by a few percent but then it slowly drops afterwards as the halo equilibrates.

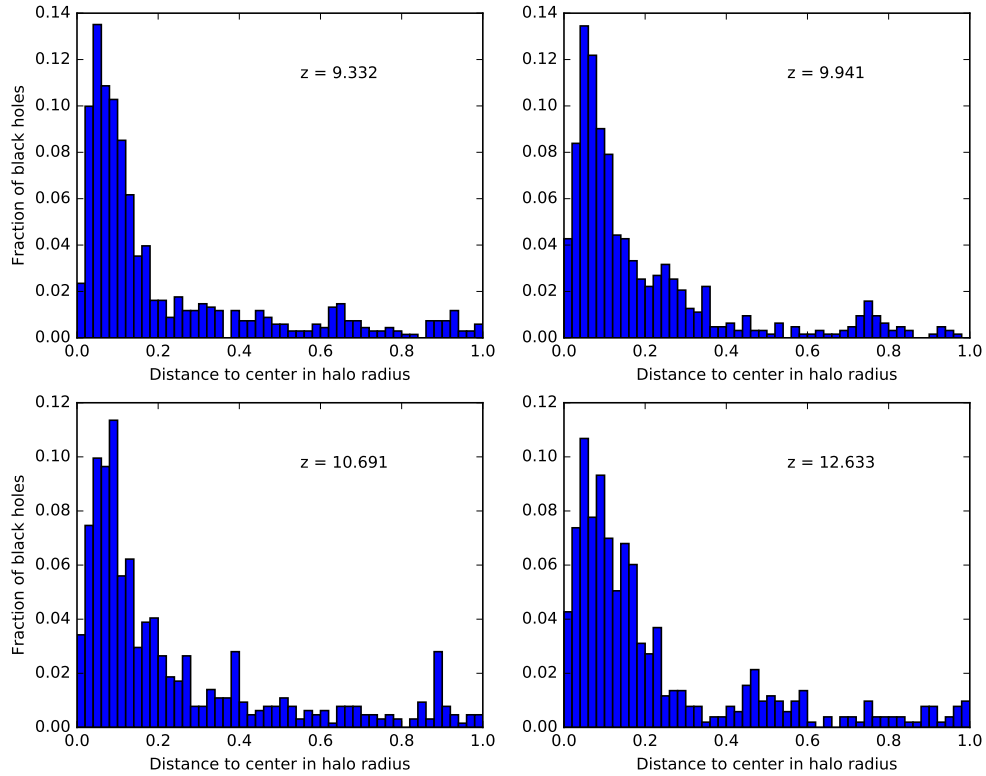


Figure 5.5: The radial distribution at four different redshifts: $z = 9.33, 9.94, 10.69, 12.63$. The majority of the black hole remnants are situated within a radius of $0.2r_{\text{vir}}$ in these snapshots.

After having a general picture of the evolution of radial distribution over time from Figure 5.4, we further inspect the full radial distribution of BHs at four redshifts: $z = 9.33, 9.94, 10.69, 12.63$ (Figure 5.5). The number of black holes in these four snapshots all surpass 500, providing a good statistical sample, and halo properties also become relatively stable at this stage.

The radial distributions in these four snapshots are overall similar, showing the bulk of the black holes existing within 20% of the virial radius, while fraction of black holes in the outskirts ($r/r_{\text{vir}} > 0.2$) of the halo are small and approximately invariant with radius. This shows that the black holes at these selected times are close to the center of the halo, but

there is a deficit in the smallest radius bin ($r/r_{\text{vir}} < 0.02$), which is indicative of the black holes’ orbits not having a high probability of passing through the center of mass of the halo. Meanwhile, this central concentration is consistent with stellar densities within the first galaxies, showing that the black holes could have similar dynamics to stellar trajectories in these early galaxies.

Because these data are only “snapshots” in time and only tell us about the instantaneous position of the black holes, we must perform an orbital analysis on the black holes to determine their dynamics and positions within their host halos. In particular by studying the evolution of the semi-major axis and eccentricity, we can understand whether they sink to the center or remain in stable orbits. This type of analysis can inform us whether these stellar-mass black holes are good candidates for black hole mergers in the first galaxies or do they remain as intermediate-mass black holes ($M_{\text{BH}} \simeq 10^2 - 10^4 M_{\odot}$).

5.3 Black hole orbital properties

As mentioned in the end of last section, to determine the evolution of their orbits, we need look past the radial distribution, which will be rapidly varying with respect to time. We perform an orbital analysis at every snapshot in the simulation and present the data from the same four times that are shown in Figure 5.5. The two primary quantities that describe an orbit are the semi-major axis and the eccentricity. As a reminder, the details about the orbital analysis are given Section 4.1.

5.3.1 Halo point mass approximation

In this first stage of analysis, we assume that the gravitational potential is spherical that is sourced from a point mass with M_{vir} (Section 4.1.1).

The fraction of black holes with semi-major axis shorter than $0.1r_{\text{vir}}$ fluctuates from 54% to over 70%, mostly above 60%. This clearly contradicts the radial distribution plot in 5.5, which shows less than half black holes are within $0.1r_{\text{vir}}$ range in all four redshifts.

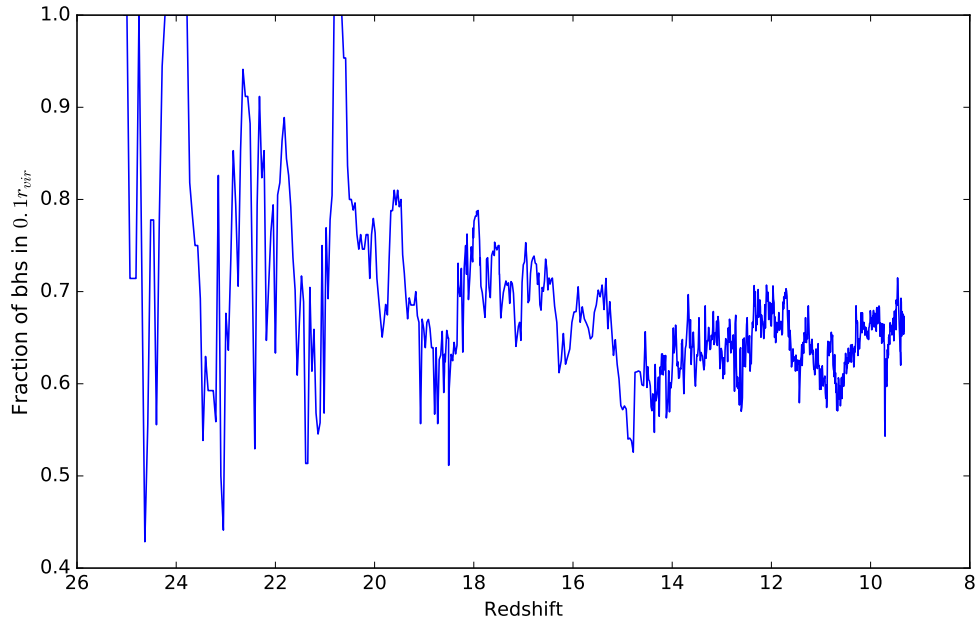


Figure 5.6: The evolution of the fraction of black holes with semi-major axes less than $0.1r_{\text{vir}}$. It fluctuates rapidly at early times when there are few black holes, but it marginally stabilizes at $z \gtrsim 14$ with the fraction between 54% and 70%.

We believe the contradiction comes from the over-simplification of approximating a halo as a point gravitational source. The point source potential is much steeper than a typical halo potential profile, thus the orbit of black holes would be much more concentrated to the center under point source potential than it would be realistically. The fraction of the semi-major axes within $0.1r_{\text{vir}}$ is slightly higher by $\sim 10\%$ than the fraction of radial distances, shown in Figure 5.5. This difference could be caused by eccentric orbits that spend more time at larger distances as their orbital speeds decrease.

The discrepancy is more evident when we look at the distribution of semi-major axis at the same four redshifts as Figure 5.5 in Figure 5.7. This figure shows the semi-major axes of the black hole remnants inside halos.

Compared to the raw radial distribution, it is more centrally concentrated because of the over-centralized point source potential : nearly all of the black holes have semi-major axes less than $0.2r_{\text{vir}}$. The total distribution over all halos do not vary much between these

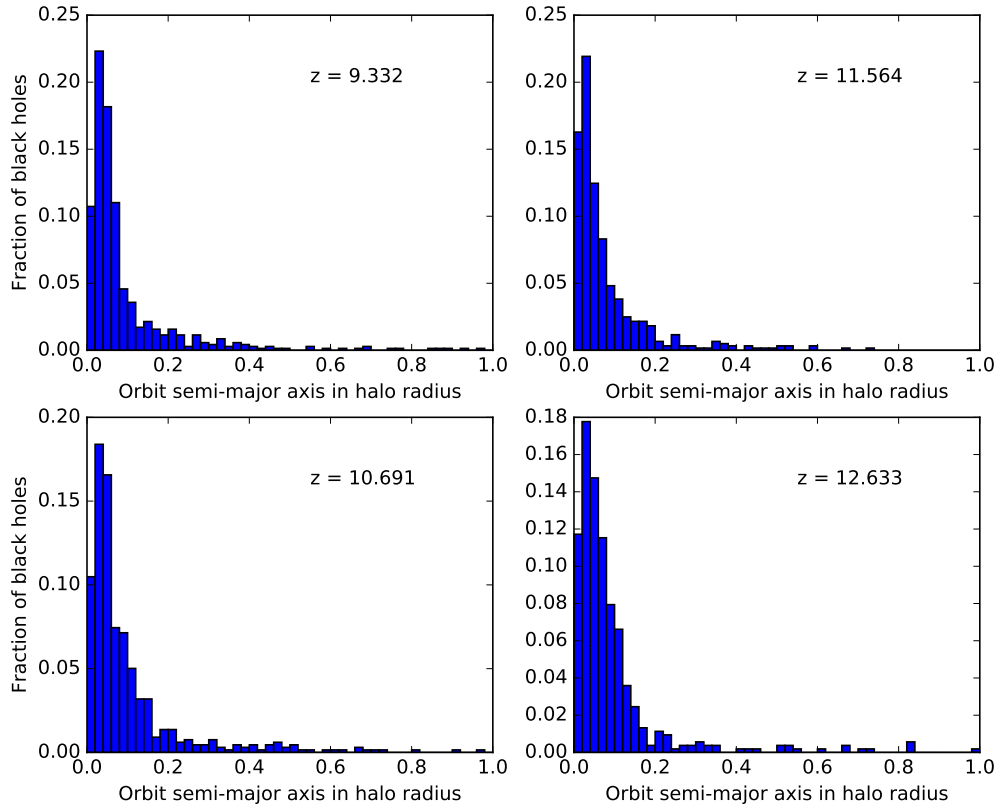


Figure 5.7: Distribution of orbital semi-major axes in point source approximation at the same four redshifts in Figure 5.5. Notice that the distribution is much more peaked as the radial distribution.

four times but it still favors the central portions of the halo, which is consistent with Figure 5.5.

From the distribution of sma alone we can already see that point source potential is a poor approximation to the real halo potentials. For completeness and comparison with simulated potential in next section, we went on to plot the distribution of eccentricity.

By calculating the eccentricities, we can determine whether the black holes spend most of their time in the central regions of the halo or travel to the outskirts or even outside of the host halo.

As suspected from comparing the radial and semi-major axis distributions, the black holes are mostly on highly eccentric orbits. Nearly all of the black holes have $e > 0.6$ with

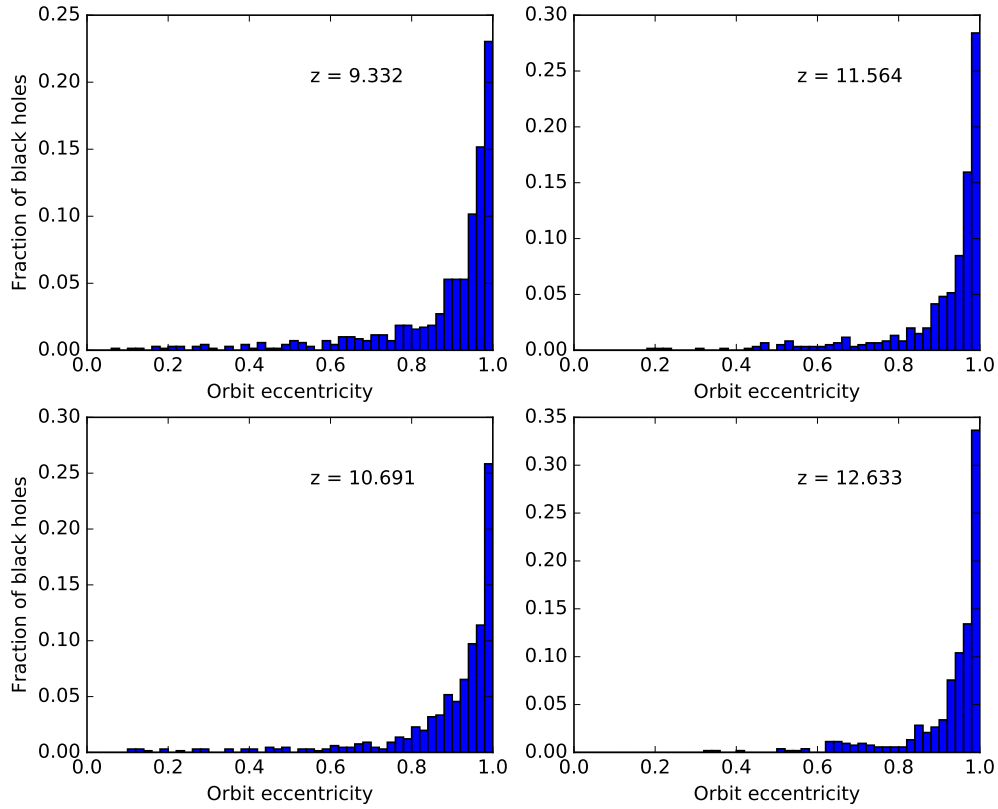


Figure 5.8: Distribution of orbital eccentricities in point source approximation at the same four redshifts in Figure 5.5. Between a quarter and one-third of the black holes are on highly eccentric orbits. We exclude any unbound black holes in these plots.

around a quarter of the population having $e > 0.95$. This implies that the black holes will have a nearly radial orbit as they plunge into the halo center. The highly eccentric orbits means that the black holes will make passages into the central regions of the halo, where the densities are higher, which will increase the effects of dynamical friction.

5.3.2 Using the simulated gravitational potential

Having shown that point source approximation did not perform well to for calculating BH orbits, we now turn to the spherically-averaged simulated gravitational potential (Section 4.1.2, as shown in Figure 5.9).

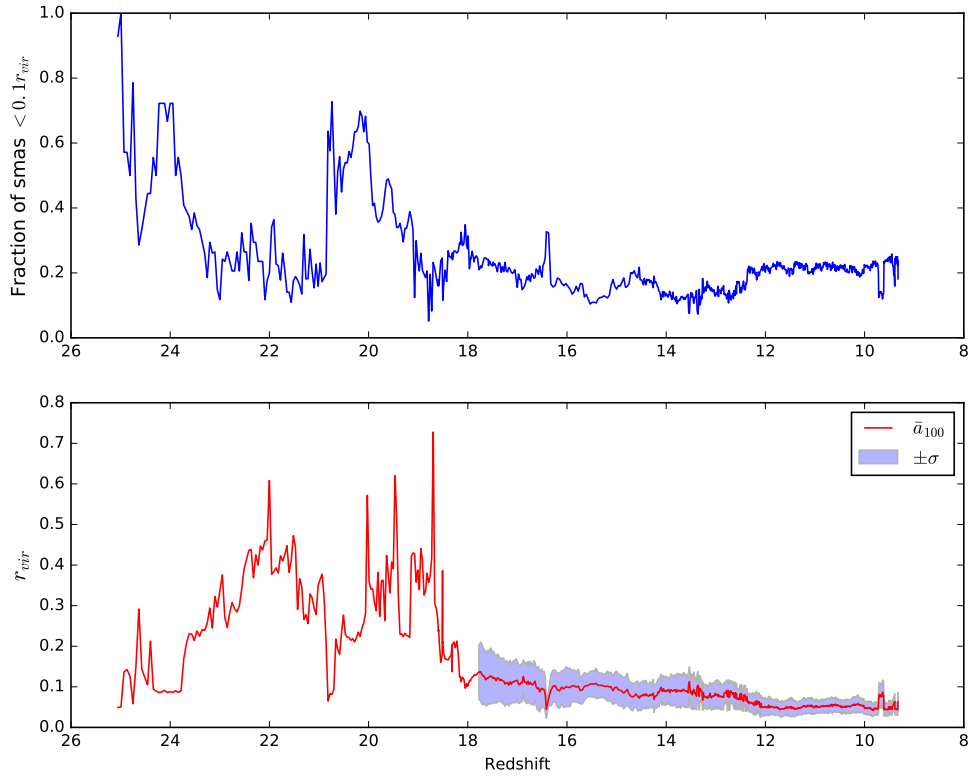


Figure 5.9: In simulated potential, orbital property stabilizes at redshift $z \lesssim 18$. From upper panel we see that about 20 percent of all black holes stay inside $0.1 r_{\text{vir}}$ from the halo center. From lower panel we see that the average of 100 shortest semi-major axis is about $0.05 r_{\text{vir}}$, with the same order of variation; and the variation kept decreasing.

When compared to our analysis with the point mass approximation, the fraction of black holes with semi-major axes below $0.1 r_{\text{vir}}$ contains less fluctuations. More importantly, these fractions are substantially decreased from 60–70% in the point-mass approximation to $\sim 20\%$ when we use the simulated potential, which is consistent with the radial position distribution shown in the upper panel of Figure 5.5.

The average semi-major axes of the 100 innermost black holes shown in the lower panel have larger fluctuations at early times ($z > 18$) but stabilize to nearly about $0.05 r_{\text{vir}}$ in the end, with standard deviation of the same order in a decreasing trend. Comparing to the average radial position of 100 innermost black holes, about $0.03 r_{\text{vir}}$, the average *sma* is

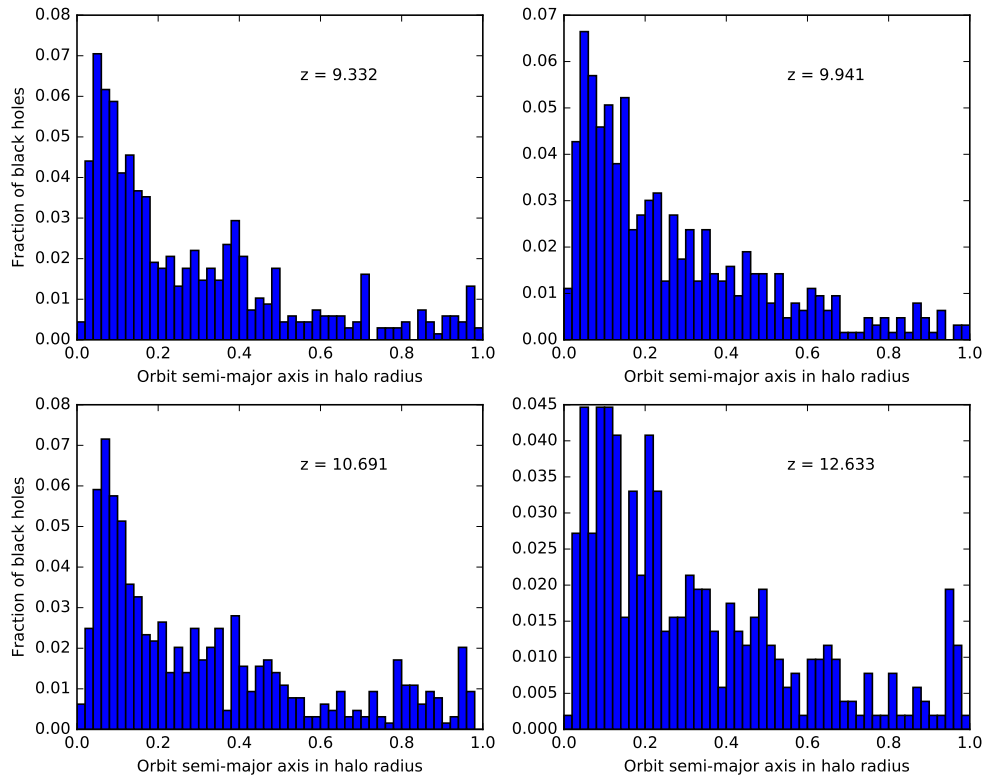


Figure 5.10: Distribution of orbital semi-major axes at the same four redshifts in Figure 5.5. Notice that the distribution is no longer as centrally peaked than the radial distribution.

slightly larger.

Figure 5.10 shows the full distribution of sma at the same four redshifts in Figure 5.5. We see that the distribution here is much less centrally concentrated than the same distribution in point source potential well (Figure 5.7). This change is caused by the shallower potential well created by the more extended mass distribution in the halo. Moreover, the distribution is also slightly less concentrated than the radial position distribution, which means the distance of most black holes are less than their orbit semi-major axes. Considering the high eccentricity of most BH orbits, this is a very reasonable result. Similarly, the total distribution over all halos still do not vary much between these four times, yet still favors the central portions of the halo.

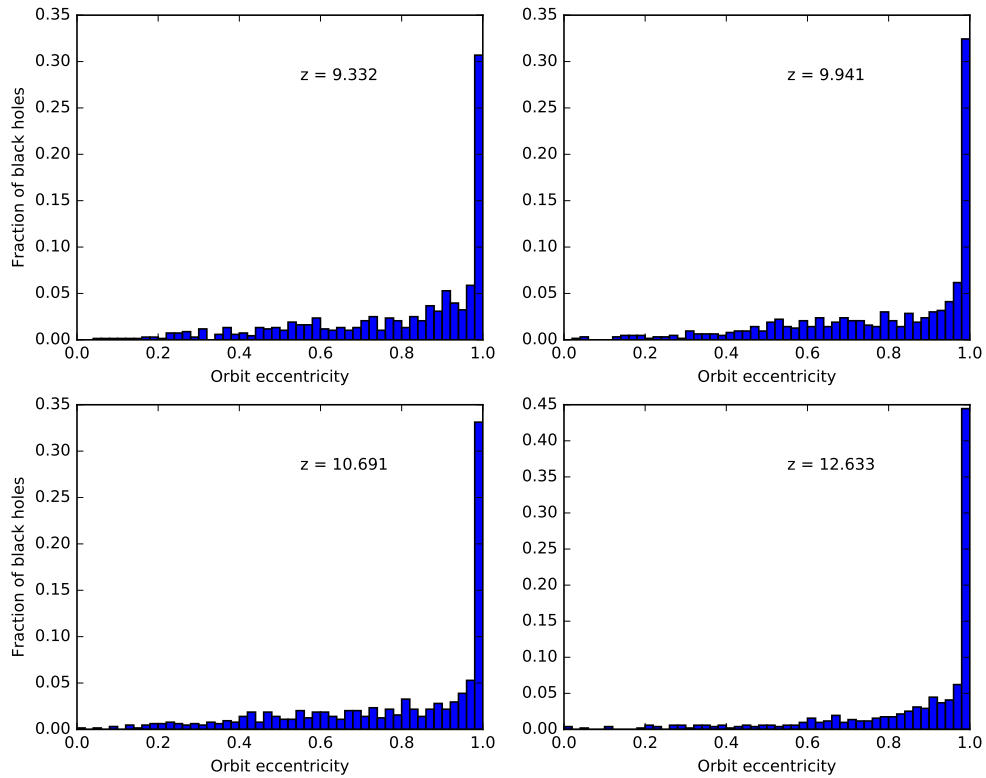


Figure 5.11: Distribution of orbital eccentricities at the same four redshifts in Figure 5.5. Between one-third and one-half of the black holes are on highly eccentric orbits. We exclude any unbound black holes in these plots.

However, there still exists a deficit in the smallest semi-major axis bin, showing that these black holes do not live in the very centers of the first galaxies. They orbit at relatively large radii when compared to the separations needed for black hole mergers if a black hole exists in the center of the halo.

Figure 5.11 shows the distribution of eccentricity at the same four redshifts. Comparing to the distribution in point source potential, we can see that the distribution of eccentricity is more skewed towards 1, which is consistent with the difference in semi-major axes distribution of the two methods. Point source potential is much steeper than the spherical average of simulated potential and thus exerts more gravitational force on the black holes, resulting

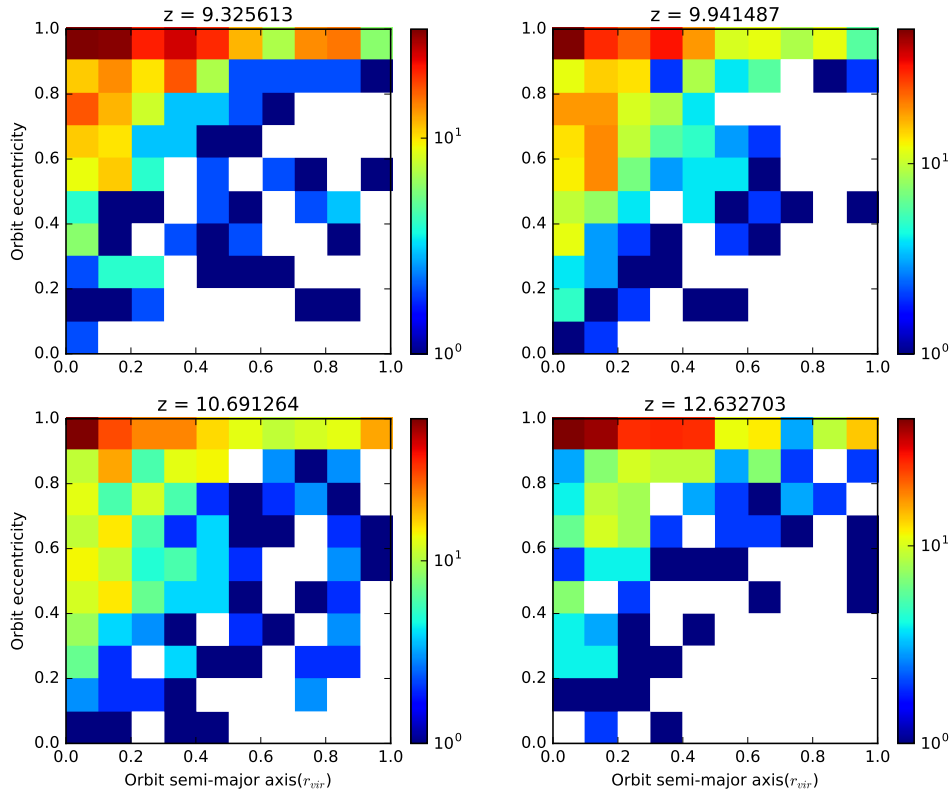


Figure 5.12: Distribution of BHs in semi-major axis-eccentricity phase space(sma-ecc) at the same four redshifts as in Figure 5.5. Color bars represent the number of BHs. We can clearly see that at all four redshifts, BHs number densities peaks at upper left corner. BHs with high eccentricity and small semi-major axes have the largest proportion.

in shorter and more circular orbits.

The large eccentricity most likely comes from the orbital angular momentum that is originally associated with the progenitor halos that merged into the main halo, and there hasn't been enough time for this angular momentum to be lost through dynamical processes, such as dynamical friction. If dynamical friction plays an important role in the orbital evolution of stellar-mass black holes, they will slowly sink toward the halo center, possibly resulting in later black hole mergers. These black holes with high eccentricities are prime candidates for mergers because they are the ones that will venture closest to the halo center and any massive black hole that might exist in the (proto-)galaxy center.

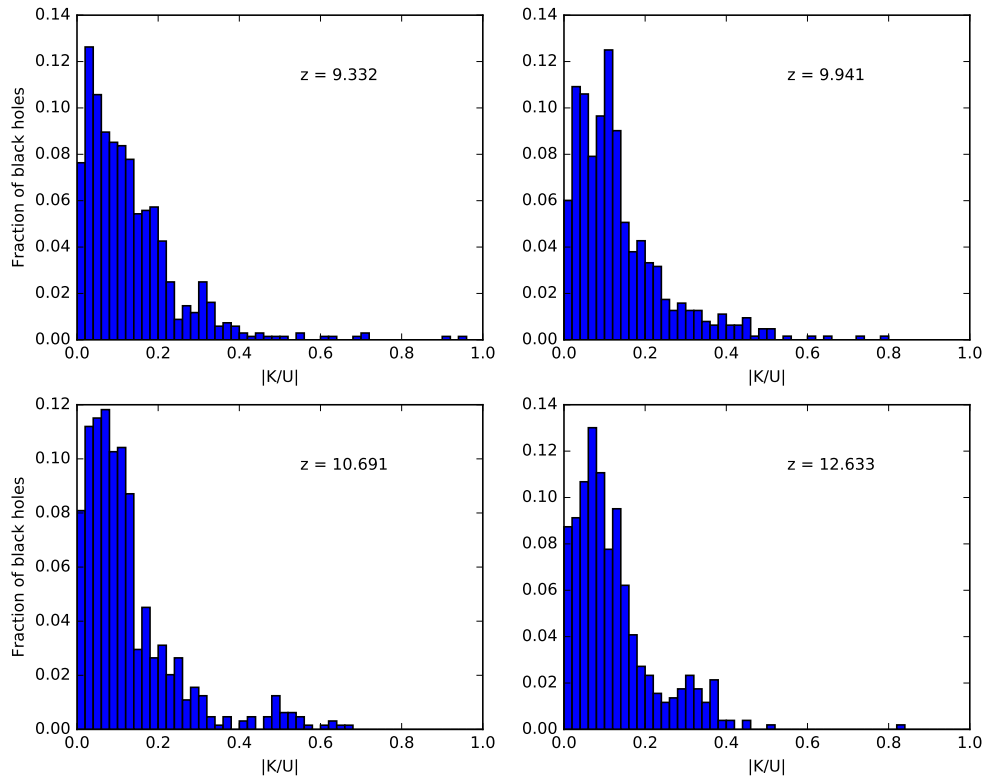


Figure 5.13: Distribution of the ratio of kinetic energy and potential energy at the same four redshifts as in Figure 5.5.

By plotting the distribution of BHs in sma-ecc phase space, we can easily see that BHs tend to reside in the upper left corner, i.e. BHs tend to have short semi-major axis and high eccentricity. According to the discussion in Section 4.2, this is the most favorable scenario for the growth of BHs, since the BHs will be able to trespass the central regions of host halo due to high eccentricity and short orbit, where the density is most likely very high in the halo. Passage into high density region will not only provide more mass for accretion on to BHs, but also exert higher dynamical friction to slow them down and keep them near the center.

We end this subsection by inspecting the kinetic to potential energy ratio for the black holes to search for any decreasing trends in the kinetic energy. A general decreasing trend

of the whole distribution could be a sign for the orbital energy loss. The potential energy slowly varies with time with the potential well deepening as it accretes matter through smooth accretion from the intergalactic medium and halo mergers. However for a single orbit, one would expect the ratio of these energies to fluctuate with maximal (minimal) kinetic energy at the pericenter (apocenter). There are no significant differences in the $|K/U|$ ratio distributions in these four redshifts. Most of the black holes have ratios lower than 0.2 with very few black holes having $|K/U| > 0.5$, which makes sense as the black holes spend most of their time at large radial distances in highly elliptical orbits. We can further analyze the evolution of the black hole orbits by a direct inspection of their angular momentum, which we perform next.

5.3.3 Angular momentum

As discussed in Section 4.2, losing angular momentum due to dynamical friction is a major cause for BHs to sink to center of halos. Given the position and velocity of BHs w.r.t to the center of host halos, we can calculate their angular momentum at each timestep and see how it evolves over time. Let \mathbf{r}_{bh} , \mathbf{v}_{bh} , \mathbf{r}_{h} , \mathbf{v}_{h} denote the position and velocity vectors of black holes and their host halos, the magnitude of (specific) angular momentum is given by

$$L = |(\mathbf{r}_{\text{bh}} - \mathbf{r}_{\text{h}}) \times (\mathbf{v}_{\text{bh}} - \mathbf{v}_{\text{h}})| \quad (5.2)$$

We were trying to do the same analysis on angular momentum as we did with the semi-major axes and eccentricity, hoping to find a decreasing trend in the angular momentum of some BHs particles and to further estimate the merger rate from the rate of decrease in angular momentum.

However, as we shall see in the plots below, there are two drawbacks that make this approach impossible for the purpose of estimating merger rate through angular momentum.

- From the analysis of eccentricity (Figure 5.11 we know that most of the BHs' orbits are highly eccentric, which means the angular momentum L in equation 5.2 is very

sensitive to the position of halo center and halo velocity. We also know from Section 2.2 that halo center coordinate is the peak density location or center of mass (in our case the latter), and halo velocity is the density weighted average of all particle velocities. This means that the halo center positions and halo velocities are not smooth functions over time due to the change of mass distribution inside halos or mergers, and thus the value of angular momentum fluctuates a lot even for slight changes in the halo center position and velocity. This is the main reason why this did not work.

- The simulation volume is not big enough. Although we have about 700 BH particles, many of them exist in halos that have experienced mergers at some point in the simulation, which are not suitable for this type of analysis. The number of BHs that reside in quiet halos (halos without merger) for long enough time to see a trend of the evolution of angular momentum (hopefully decreasing) is too small to draw any statistical conclusion.

One technique that can reduce the noisiness is to iteratively calculate the center of mass of the part enclosed by the a shrinking sphere until the result converges, but the result is still not good enough for the purpose of this work

Figure 5.14 illustrate how much the discontinuity in the halo center position can be amplified in the BH angular momentum. This black hole stays in a halo without major merger for over 500 timesteps from redshift $z \sim 16$ to $z \sim 9$, which is the second longest one in the simulation. It is worth noting that the halo center position curve in the figure is already optimized using the shrinking sphere technique mentioned above.

The first panel shows the BH angular momentum, which is very noisy. The middle three panels shows the x, y, z coordinate of halo center and the black hole in code unit. We can see that the BH coordinate varies in a smooth curve, while halo center position undergoes slight fluctuation in x coordinate, and has tiny jitteries that are barely discernible in y and z coordinates. However when we look at the relative position of the BH w.r.t the halo in the bottom panel, we see that there are two series of significant noisy peaks whose

redshift coordinates coincide with the most noisy part of the angular momentum curve, in the middle between redshift 10 and 11.

The smoothness of BH coordinates curve indicates that this noisiness in BH angular momentum is solely because of the discontinuity of halo center position, which is inevitable given how these halos are identified numerically. Even if the halo center fluctuates only a few percent, for black holes that are close to the center, e.g. with $sma < 0.1r_{\text{vir}}$, the difference is still significant.

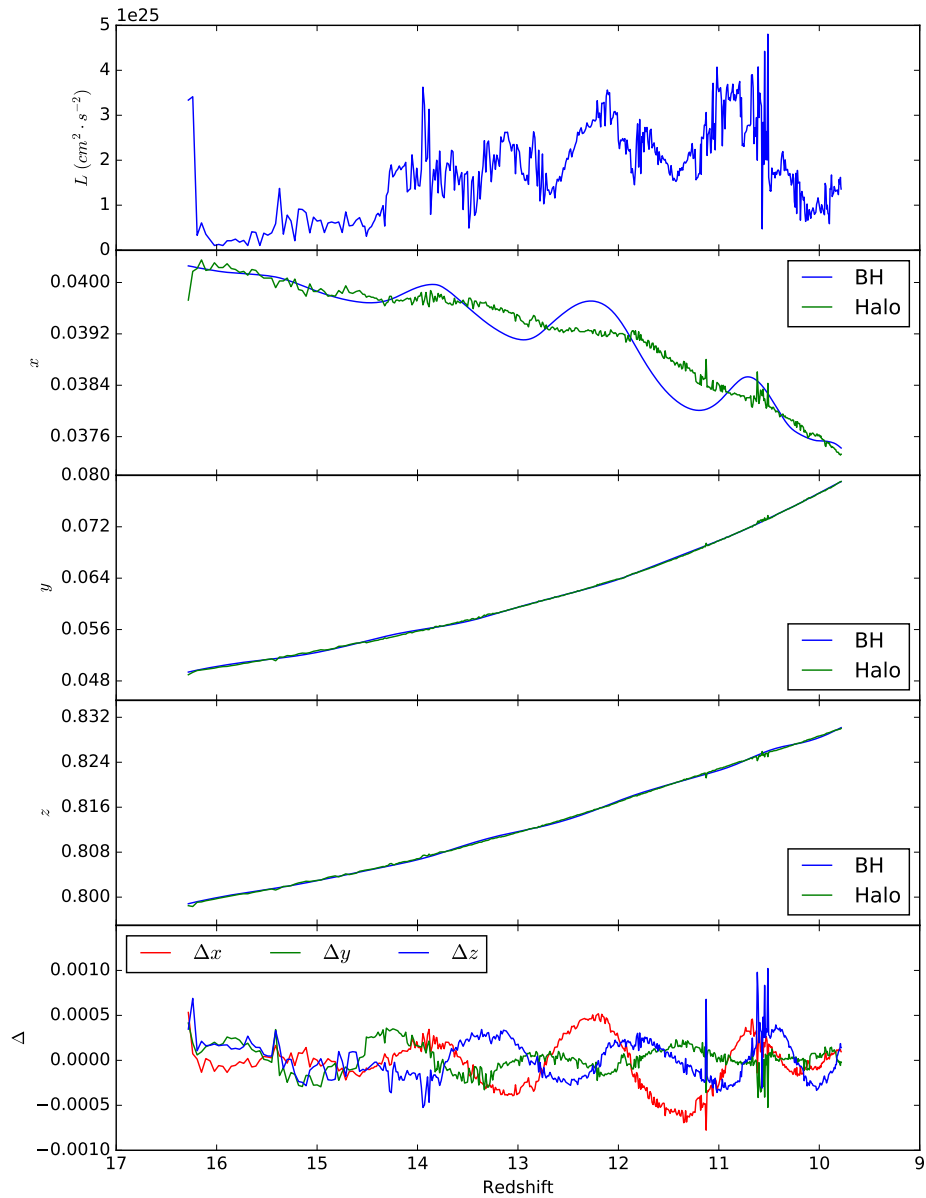


Figure 5.14: This figure illustrates the reason why angular momentum is so noisy. The first panel is the angular momentum. The following three panels are the x , y , and z coordinates of halo center and BH position. We see there is slight jitter in x coordinate of halo center. Fluctuations in y and z coordinates are barely discernible. The BH coordinates are all very smooth. The lowest panel shows the noisiness of relative position between BH and halo.

CHAPTER 6

CONCLUSIONS AND FUTURE WORK

6.1 Conclusions

In order to study seed black hole formation and evolution, we ran a cosmological simulation that incorporated star formation, stellar feedback and Lyman-Werner radiation background. We evolve a comoving simulation volume of 1 Mpc^3 from redshift $z \sim 130$, and output over 800 data sets from redshift $z \sim 16$ to $z \sim 9$, about one per 0.5 Myr. We then find all the DM halos in each snapshot with ROCKSTAR and extract all seed BHs that reside in halos and calculate their orbits in spherically-averaged potential field characterized by semi-major axis and eccentricity.

The first seed BH appeared at $z \sim 25$, and the number steadily grow into around 700 after $z \sim 10$ (Figure 5.1). Most black holes exist in minihalos with masses $M_{\text{BH}} > 10^6 M_{\odot}$ (Figure 5.2), which is consistent with their birthplaces. Halos in higher mass range tend to have higher number of BHs per halo (Figure 5.3).

In order to calculate orbital properties, we use point mass potential and spherical average of simulated potential to approximate the potential field. They both have spherical symmetry which allows us to solve for semi-major axis and eccentricity from simple equations. Point mass potential turned out to be a bad approximation since its potential well is much steeper than an extended halo potential, resulting in over-concentration around the center of halos, contradicting the actual radial distribution (Figure 5.5, 5.7). Spherical average on the other hand is a much better approximation. In this potential, about 20% of all black holes have semi-major axes (sma) less than $0.1 r_{\text{vir}}$, and the average of 100 smallest sma drops to about $0.05 r_{\text{vir}}$ at $z \sim 9$. Between one-third and one-half black holes are on highly eccentric orbits, with $ecc > 0.95$. BHs with both of these properties comprise a significant

percentage (around 10%, Figure 5.12) of the whole population, and are primary candidates for sinking to the halo center. Although some black holes might sink to the center, the dynamical friction timescale is comparable to the Hubble time. This suggests that most stellar mass black holes will not migrate to the center, co-existing with the stellar population of the galaxy.

A further goal of this work is to estimate the merger rate from the sample of seed BHs through loss rate of angular momentum. The angular momentum is calculated as the cross product of relative position and relative velocity between BH and halo center. Unlike the BH positions which are calculated self-consistently from the hydrodynamic and Poisson equations, halo centers are artificially assigned as density peak or center of mass, either of which result in jitteries in their position and velocity evolution. Furthermore, since many BHs have small sma and high ecc , their angular momentum are very sensitive in discontinuity of halo center positions. Therefore, BHs angular momentum w.r.t. halo center defined this way is too noisy for calculating merger rate (Figure 5.14). Possible remedies is proposed below in Section 6.2.

6.2 Future work

There are several possible routes along which this work can be improved.

- We may reduce the nosiness in angular momentum by using minimum location of potential field instead of center of mass of halo. First, potential field is born to be much more smoother than density field (consider a point mass and its potential field). Second, it's potential field that directly interact with BHs keeps them orbitting around instead of density field. Using potential field seems more natural. Lastly, potential field in the simuation is calculated self-consistenly from mathematically rigorous Poisson equation, carrying much less artifact than halo-finding process. This way, we may have a better chance to calculate merger rates of BHs properly.

- The BHs in this simulation are inert. They do not accrete mass or generate feedback, which is part of the reason why the dynamical friction time scale is so long. We can add accretion and feedback module into the simulation. This will inevitably increase computing time, but we will have a clearer picture of how accretion and feedback affect the orbits of BHs, which might either increase or decrease the dynamical friction time scale.
- We may increase the simulation volume to include more BHs and massive halos that host BHs. Larger samples can give more statistically justified results with less uncertainties.

Black hole formation and evolution has long been an active field and difficult problem to tackle for the lack of observation and associated extreme physical properties. For all the progress made during the past decades in the field of black hole formation and evolution, many mysteries still remain. With more advanced observation telescopes such as James-Webb Space Telescope launching soon, and ever-increasing computing power, I am sure more and more exciting discoveries will be made in this area in the near future.

REFERENCES

1. A. S. Eddington, *MNRAS* **90**, 668–678 (May 1930).
2. S. Chandrasekhar, *MNRAS* **95**, 207–225 (Jan. 1935).
3. J. R. Oppenheimer, G. M. Volkoff, *Physical Review* **55**, 374–381 (Feb. 1939).
4. C. K. Seyfert, *ApJ* **97**, 28 (Jan. 1943).
5. H. C. Ford *et al.*, *ApJL* **435**, L27–L30 (Nov. 1994).
6. R. J. Harms *et al.*, *ApJL* **435**, L35–L38 (Nov. 1994).
7. H. J. Smith, D. Hoffleit, *Nature* **198**, 650–651 (May 1963).
8. O. J. Eggen, A. R. Sandage, *ApJ* **140**, 130 (July 1964).
9. J. L. Greenstein, M. Schmidt, *ApJ* **140**, 1 (July 1964).
10. A. G. W. Cameron, *Nature* **194**, 963–964 (June 1962).
11. F. Hoyle, W. A. Fowler, *MNRAS* **125**, 169 (1963).
12. G. B. Field, *ApJ* **140**, 1434 (Nov. 1964).
13. G. A. Harrower, *ApJ* **132**, 22 (July 1960).
14. Y. B. Zel’dovich, I. D. Novikov, *Soviet Physics Doklady* **9**, 246 (Oct. 1964).
15. E. E. Salpeter, *ApJ* **140**, 796–800 (Aug. 1964).
16. D. Lynden-Bell, *Nature* **223**, 690–694 (Aug. 1969).
17. A. Hewish, S. J. Bell, J. D. H. Pilkington, P. F. Scott, R. A. Collins, *Nature* **217**, 709–713 (Feb. 1968).
18. R. J. Brucato, J. Kristian, *ApJL* **173**, L105 (May 1972).
19. C. T. Bolton, *Nature* **235**, 271–273 (Feb. 1972).
20. H. Mauder, *A&A* **28**, 473 (Nov. 1973).

21. C. E. Rhoades, R. Ruffini, *Physical Review Letters* **32**, 324–327 (Feb. 1974).
22. B. Balick, R. L. Brown, *ApJ* **194**, 265–270 (Dec. 1974).
23. R. Genzel *et al.*, *Nature* **425**, 934–937 (Oct. 2003).
24. A. M. Ghez *et al.*, *ApJ* **620**, 744–757 (Feb. 2005).
25. L. Ferrarese, D. Merritt, *ApJL* **539**, L9–L12 (Aug. 2000).
26. K. Gebhardt *et al.*, *ApJL* **539**, L13–L16 (Aug. 2000).
27. S. Tremaine *et al.*, *ApJ* **574**, 740–753 (Aug. 2002).
28. K. Gültekin *et al.*, *ApJ* **698**, 198–221 (June 2009).
29. J. Magorrian *et al.*, *AJ* **115**, 2285–2305 (June 1998).
30. N. Häring, H.-W. Rix, *ApJL* **604**, L89–L92 (Apr. 2004).
31. A. Marconi *et al.*, *MNRAS* **351**, 169–185 (June 2004).
32. A. Lawrence *et al.*, *MNRAS* **379**, 1599–1617 (Aug. 2007).
33. D. J. Mortlock *et al.*, *Nature* **474**, 616–619 (June 2011).
34. M. J. Rees, *ARA&A* **22**, 471–506 (1984).
35. V. Bromm, P. S. Coppi, R. B. Larson, *ApJL* **527**, L5–L8 (Dec. 1999).
36. V. Bromm, P. S. Coppi, R. B. Larson, *ApJ* **564**, 23–51 (Jan. 2002).
37. T. Abel, G. L. Bryan, M. L. Norman, *ApJ* **540**, 39–44 (Sept. 2000).
38. N. Yoshida, K. Omukai, L. Hernquist, T. Abel, *ApJ* **652**, 6–25 (Nov. 2006).
39. K. Omukai, R. Nishi, H. Uehara, H. Susa, *Progress of Theoretical Physics* **99**, eprint: astro-ph/9809232 (May 1998).
40. E. Ripamonti, F. Haardt, A. Ferrara, M. Colpi, *MNRAS* **334**, 401–418 (Aug. 2002).
41. J. C. Tan, C. F. McKee, *ApJ* **603**, 383–400 (Mar. 2004).
42. W. Zhang, S. E. Woosley, A. Heger, *ApJ* **679**, 639–654 (May 2008).

43. J. R. Bond, W. D. Arnett, B. J. Carr, *ApJ* **280**, 825–847 (May 1984).
44. C. L. Fryer, V. Kalogera, *ApJ* **554**, 548–560 (June 2001).
45. C. F. McKee, J. C. Tan, *ApJ* **681**, 771–797 (July 2008).
46. D. Spolyar, K. Freese, P. Gondolo, *Physical Review Letters* **100**, 051101 (Feb. 2008).
47. K. Freese, P. Bodenheimer, D. Spolyar, P. Gondolo, *ApJL* **685**, L101 (Oct. 2008).
48. M. G. Haehnelt, M. J. Rees, *MNRAS* **263**, 168–178 (July 1993).
49. A. Loeb, F. A. Rasio, *ApJ* **432**, 52–61 (Sept. 1994).
50. D. J. Eisenstein, A. Loeb, *ApJ* **443**, 11–17 (Apr. 1995).
51. V. Bromm, A. Loeb, *ApJ* **596**, 34–46 (Oct. 2003).
52. S. M. Koushiappas, J. S. Bullock, A. Dekel, *MNRAS* **354**, 292–304 (Oct. 2004).
53. M. C. Begelman, M. Volonteri, M. J. Rees, *MNRAS* **370**, 289–298 (July 2006).
54. G. Lodato, P. Natarajan, *MNRAS* **371**, 1813–1823 (Oct. 2006).
55. I. Shlosman, J. Frank, M. C. Begelman, *Nature* **338**, 45–47 (Mar. 1989).
56. L. Mayer, S. Kazantzidis, A. Escala, S. Callegari, *Nature* **466**, 1082–1084 (Aug. 2010).
57. M. C. Begelman, E. M. Rossi, P. J. Armitage, *MNRAS* **387**, 1649–1659 (July 2008).
58. M. Volonteri, G. Lodato, P. Natarajan, *MNRAS* **383**, 1079–1088 (Jan. 2008).
59. R. Schneider, K. Omukai, A. K. Inoue, A. Ferrara, *MNRAS* **369**, 1437–1444 (July 2006).
60. P. C. Clark, S. C. O. Glover, R. S. Klessen, *ApJ* **672**, 757–764 (Jan. 2008).
61. B. Devecchi, M. Volonteri, *ApJ* **694**, 302–313 (Mar. 2009).
62. S. F. Portegies Zwart, J. Makino, S. L. W. McMillan, P. Hut, *A&A* **348**, 117–126 (Aug. 1999).
63. B. Davies *et al.*, *MNRAS* **416**, 972–990 (Sept. 2011).

64. Y. B. Zel'dovich, I. D. Novikov, *Soviet Astronomy* **10**, 602 (Feb. 1967).
65. S. W. Hawking, *Physical Review Letters* **26**, 1344–1346 (May 1971).
66. M. Y. Khlopov, S. G. Rubin, A. S. Sakharov, *Astroparticle Physics* **23**, 265–277 (Mar. 2005).
67. D. N. Page, S. W. Hawking, *ApJ* **206**, 1–7 (May 1976).
68. C. Alcock *et al.*, *ApJ* **542**, 281–307 (Oct. 2000).
69. P. Tisserand *et al.*, *A&A* **469**, 387–404 (July 2007).
70. M. Ricotti, N. Y. Gnedin, J. M. Shull, *ApJ* **685**, 21–39 (Sept. 2008).
71. C. Lacey, S. Cole, *MNRAS* **262**, 627–649 (June 1993).
72. W. H. Press, P. Schechter, *ApJ* **187**, 425–438 (Feb. 1974).
73. R. H. Wechsler, J. S. Bullock, J. R. Primack, A. V. Kravtsov, A. Dekel, *ApJ* **568**, 52–70 (Mar. 2002).
74. A. J. Benson, *Physics Reports* **495**, 33–86 (Oct. 2010).
75. M. Volonteri, F. Haardt, P. Madau, *ApJ* **582**, 559–573 (Jan. 2003).
76. M. Volonteri, S. Callegari, M. Colpi, M. Dotti, L. Mayer, *Mem. Societa Astronomica Italiana* **79**, 1231 (2008).
77. C. A. Baker *et al.*, *Physical Review Letters* **98**, 149102 (Apr. 2007).
78. B. J. Kelly, W. Tichy, M. Campanelli, B. F. Whiting, *Phys. Rev. D* **76**, 024008 (July 2007).
79. M. González, E. Audit, P. Huynh, *A&A* **464**, 429–435 (Mar. 2007).
80. M. Volonteri, J. Bellovary, *Reports on Progress in Physics* **75**, 124901 (Dec. 2012).
81. J.-h. Kim *et al.*, *ApJS* **210**, 14 (Jan. 2014).
82. C. M. Booth, J. Schaye, *MNRAS* **398**, 53–74 (Sept. 2009).
83. T. Okamoto, L. Gao, T. Theuns, *MNRAS* **390**, 920–928 (Nov. 2008).

84. T. Di Matteo, J. Colberg, V. Springel, L. Hernquist, D. Sijacki, *ApJ* **676**, 33–53 (Mar. 2008).
85. H. Bondi, F. Hoyle, *MNRAS* **104**, 273 (1944).
86. H. Bondi, *MNRAS* **112**, 195 (1952).
87. M. A. Alvarez, J. H. Wise, T. Abel, *ApJL* **701**, L133–L137 (Aug. 2009).
88. M. Jeon *et al.*, *ApJ* **754**, 34 (July 2012).
89. J. H. Kim, J. H. Wise, M. A. Alvarez, T. Abel, *ApJ*, *In preparation* (June 2011).
90. H. Xu, J. H. Wise, M. L. Norman, *ApJ* **773**, 83 (Aug. 2013).
91. J. A. Regan *et al.*, *Nature Astronomy* **1**, 0075 (Mar. 2017).
92. T. Kitayama, N. Yoshida, H. Susa, M. Umemura, *ApJ* **613**, 631–645 (Oct. 2004).
93. D. Whalen, T. Abel, M. L. Norman, *ApJ* **610**, 14–22 (July 2004).
94. T. Abel, J. H. Wise, G. L. Bryan, *ApJL* **659**, L87–L90 (Apr. 2007).
95. G. L. Bryan *et al.*, *ApJS* **211**, 19 (Apr. 2014).
96. M. J. Berger, P. Colella, *Journal of Computational Physics* **82**, 64–84 (May 1989).
97. M. Berger, I. Rigoutsos, *IEEE Transactions on Systems, Man and Cybernetics* **21**, 1278–1286 (Sept. 1991).
98. P. Colella, P. R. Woodward, *Journal of Computational Physics* **54**, 174–201 (Sept. 1984).
99. G. L. Bryan, M. L. Norman, J. M. Stone, R. Cen, J. P. Ostriker, *Computer Physics Communications* **89**, 149–168 (Aug. 1995).
100. B. V. Leer, *Journal of Computational Physics* **23**, 276–299 (1977).
101. P. Wang, T. Abel, W. Zhang, *The Astrophysical Journal Supplement Series* **176**, 467 (2008).
102. P. Wang, T. Abel, *ApJ* **696**, 96–109 (May 2009).
103. D. C. Collins, H. Xu, M. L. Norman, H. Li, S. Li, *ApJS* **186**, 308–333 (Feb. 2010).

104. J. M. Stone, M. L. Norman, *ApJS* **80**, 753–790 (June 1992).
105. J. M. Stone, M. L. Norman, *ApJS* **80**, 791 (June 1992).
106. R. W. Hockney, J. W. Eastwood, *Computer simulation using particles*.
107. C. L. Sarazin, R. E. White III, *ApJ* **320**, 32–48 (Sept. 1987).
108. G. J. Ferland *et al.*, *PASP* **110**, 761–778 (July 1998).
109. B. Smith, S. Sigurdsson, T. Abel, *MNRAS* **385**, 1443–1454 (Apr. 2008).
110. B. D. Smith, E. J. Hallman, J. M. Shull, B. W. O’Shea, *ApJ* **731**, 6 (Apr. 2011).
111. R. Cen, J. P. Ostriker, *ApJL* **399**, L113–L116 (Nov. 1992).
112. R. C. Kennicutt Jr., *ApJ* **344**, 685–703 (Sept. 1989).
113. A. Knebe *et al.*, *MNRAS* **415**, 2293–2318 (Aug. 2011).
114. M. Davis, G. Efstathiou, C. S. Frenk, S. D. M. White, *ApJ* **292**, 371–394 (May 1985).
115. S. More, A. V. Kravtsov, N. Dalal, S. Gottlöber, *ApJS* **195**, 4 (July 2011).
116. D. J. Eisenstein, P. Hut, *ApJ* **498**, 137–142 (May 1998).
117. J. J. Monaghan, J. C. Lattanzio, *A&A* **149**, 135–143 (Aug. 1985).
118. P. S. Behroozi, R. H. Wechsler, C. Conroy, *ApJ* **770**, 57 (June 2013).
119. M. Tegmark *et al.*, *ApJ* **474**, 1–+ (Jan. 1997).
120. B. W. O’Shea, M. L. Norman, *ApJ* **673**, 14–33 (Jan. 2008).
121. J. K. Truelove *et al.*, *ApJL* **489**, L179+ (Nov. 1997).
122. O. Hahn, T. Abel, *MNRAS* **415**, 2101–2121 (Aug. 2011).
123. Planck Collaboration, others, *A&A* **580**, A13 (Aug. 2015).
124. T. Abel, P. Anninos, Y. Zhang, M. L. Norman, *New Astronomy* **2**, 181–207 (Aug. 1997).

125. P. Anninos, Y. Zhang, T. Abel, M. L. Norman, *New Astronomy* **2**, 209–224 (Aug. 1997).
126. M. E. Machacek, G. L. Bryan, T. Abel, *ApJ* **548**, 509–521 (Feb. 2001).
127. J. H. Wise, T. Abel, *ApJ* **671**, 1559–1567 (Dec. 2007).
128. J. H. Wise, T. Abel, *ApJ* **629**, 615–624 (Aug. 2005).
129. M. Trenti, M. Stiavelli, J. M. Shull, *ApJ* **700**, 1672–1679 (Aug. 2009).
130. B. T. Draine, F. Bertoldi, *ApJ* **468**, 269–+ (Sept. 1996).
131. J. Wolcott-Green, Z. Haiman, G. L. Bryan, *MNRAS* **418**, 838–852 (Dec. 2011).
132. J. H. Wise, T. Abel, *ApJ* **684**, 1–17 (Sept. 2008).
133. T. Abel, G. L. Bryan, M. L. Norman, *Science* **295**, 93–98 (Jan. 2002).
134. B. W. O’Shea, M. L. Norman, *ApJ* **654**, 66–92 (Jan. 2007).
135. K. Omukai, Y. Yoshii, *ApJ* **599**, 746–758 (Dec. 2003).
136. G. Chabrier, *PASP* **115**, 763–795 (July 2003).
137. M. J. Turk, T. Abel, B. O’Shea, *Science* **325**, 601– (July 2009).
138. T. H. Greif, S. D. M. White, R. S. Klessen, V. Springel, *ApJ* **736**, 147 (Aug. 2011).
139. H. Susa, *ApJ* **773**, 185 (Aug. 2013).
140. H. Susa, K. Hasegawa, N. Tominaga, *ApJ* **792**, 32 (Sept. 2014).
141. C. Safranek-Shrader, V. Bromm, M. Milosavljević, *ApJ* **723**, 1568–1582 (Nov. 2010).
142. T. Abel, B. D. Wandelt, *MNRAS* **330**, L53–L56 (Mar. 2002).
143. J. H. Wise, T. Abel, *MNRAS* **414**, 3458–3491 (July 2011).
144. K. M. Górski *et al.*, *ApJ* **622**, 759–771 (Apr. 2005).
145. D. Schaerer, *A&A* **382**, 28–42 (Jan. 2002).
146. K. Nomoto, N. Tominaga, H. Umeda, C. Kobayashi, K. Maeda, *Nuclear Physics A* **777**, 424–458 (Oct. 2006).

147. A. Heger, S. E. Woosley, *ApJ* **567**, 532–543 (Mar. 2002).
148. T. H. Greif, J. L. Johnson, V. Bromm, R. S. Klessen, *ApJ* **670**, 1–14 (Nov. 2007).
149. J. H. Wise, R. Cen, *ApJ* **693**, 984–999 (Mar. 2009).
150. E. C. Ostriker, *ApJ* **513**, 252–258 (Mar. 1999).
151. K. Park, T. Bogdanović, *ApJ* **838**, 103 (Apr. 2017).
152. R. K. Sheth, G. Tormen, *MNRAS* **308**, 119–126 (Sept. 1999).
153. J. H. Wise, M. J. Turk, M. L. Norman, T. Abel, *ApJ* **745**, 50 (Jan. 2012).

VITA

Chao Shi was born in Guangde County, Anhui Province, China in 1988. Brought up by a high school teacher, his father cultivated his interest in math and science and early on. After graduating high school, he entered University of Science and Technology of China in Hefei, Anhui. Starting with computer science major, he later transfer to physics major after two years. He graduated with physics major 3 years later in 2010 and came to U.S. pursuing a PhD in the same field. After trying out condensed matter physics and nonlinear dynamics, he chose computational cosmology as his Phd thesis direction, working with Professor John Wise. He got his PhD in physics in 2017 along with a Master in Computational Science and Engineering. He would continue his career as a software engineer. In his spare time, Chao Shi loves to play badminton, running, and weight lifting.